

Bow shocks, bow waves, and dust waves

William J. Henney & S. Jane Arthur

Instituto de Radioastronomía y Astrofísica, Universidad Nacional Autónoma de México, Apartado Postal 3-72, 58090 Morelia, Michoacán, México

Accepted XXX. Received YYY; in original form ZZZ

ABSTRACT

Dust waves and bow waves result from the action of a star's radiation pressure on a stream of dusty plasma that flows past it. They are an alternative mechanism to hydrodynamic bow shocks for explaining the curved arcs of infrared emission seen around some stars. When gas and grains are perfectly coupled, for a broad class of stellar parameters, wind-supported bow shocks predominate when the ambient density is below 100 cm^{-3} to 1000 cm^{-3} . At higher densities radiation-supported bows can form, tending to be optically thin bow waves around B stars, or optically thick bow shocks around early O stars. The radiation field is sufficiently strong to overcome the collisional coupling between grains and gas at a *rip-point*, where the ratio of radiation pressure to gas pressure exceeds a critical value of roughly 1000. When the rip point occurs outside the hydrodynamic bow shock, a separate dust wave may form, decoupled from the gas shell, which can either be drag-confined or inertia-confined, depending on the stream density and relative velocity. In the drag-confined case, there is a minimum stream velocity of roughly 60 km s^{-1} that allows a steady-state stagnant drift solution for the dust wave apex. For lower relative velocities, the dust dynamics close to the axis exhibit a limit cycle behavior (rip and snap back) between two different radii. Strong coupling of charged grains to the plasma's magnetic field can modify these effects, but for a quasi-parallel field orientation the results are qualitatively similar. For a quasi-perpendicular field, on the other hand, the formation of a decoupled dust wave is strongly suppressed.

Key words: circumstellar matter – radiation: dynamics – stars: winds, outflows

1 INTRODUCTION

Curved emission arcs around stars (e.g., Gull & Sofia 1979) are often interpreted as *bow shocks*, due to a supersonic hydrodynamic interaction between the star's wind and an external stream. This stream may be due to the star's own motion or to an independent flow, such as an H II region in the champagne phase (Tenorio-Tagle 1979), or another star's wind (Canto et al. 1996). However, an alternative interpretation in some cases may be a radiation-pressure driven bow wave, as first proposed by van Buren & McCray (1988, §vi). In this scenario, photons emitted by the star are absorbed by dust grains in the incoming stream, with the resultant momentum transfer being sufficient to decelerate and deflect the grains within a certain distance from the star, forming a dust-free, bow-shaped cavity with an enhanced dust density at its edge.

Two regimes are possible, depending on the strength of coupling between the gas (or plasma) and the dust. In the strong-coupling regime, gas-grain drag decelerates the gas along with the dust. If the stream is optically thin to the star's ultraviolet radiation, then the deceleration occurs gradually over a range of radii, forming a relatively thick shell. On the other hand, if the stream is optically thick, then a shocked gas shell forms in a similar fashion to the wind-driven bow shock case, except internally supported by trapped radiation instead of shocked stellar wind. In the weak-coupling regime, the gas stream is relatively unaffected and the dust temporarily decouples to

form a dust-only shell. This second case has recently been studied in detail in the context of the interaction of late O-type stars (some of which have very weak stellar winds) with dusty photoevaporation flows inside H II regions (Ochsendorf et al. 2014b,a; Ochsendorf & Tielens 2015). We follow the nomenclature proposed by Ochsendorf et al. (2014a), in which *dust wave* refers to the weak coupling case and *bow wave* to the strong coupling case. More complex, hybrid scenarios are also possible, such as that studied by van Marle et al. (2011), where a hydrodynamic bow shock forms, but the larger dust grains that accompany the stellar wind pass right through the shocked gas shell, and form their own dust wave at a larger radius.

In this paper, we develop simple physical models to show in detail when and how these different interaction regimes apply when varying the parameters of the star, the dust grains, and the ambient stream. We concentrate primarily on the case of luminous early type stars, where dust is present only in the ambient stream, and not in the stellar wind. The paper is organized as follows. In § 2 we consider the case where the grains are perfectly coupled to the gas via collisions, investigating the relative importance of wind and radiation in providing internal support for the bow shell as a function of the density and velocity of the ambient stream, as well as calculating the shell's ionization state and radiative cooling efficiency. In § 3 we calculate in detail the grain charging and dynamics, subject to radiation and drag forces, in order to determine the rip point where gas-grain coupling catastrophically breaks down. This is used to

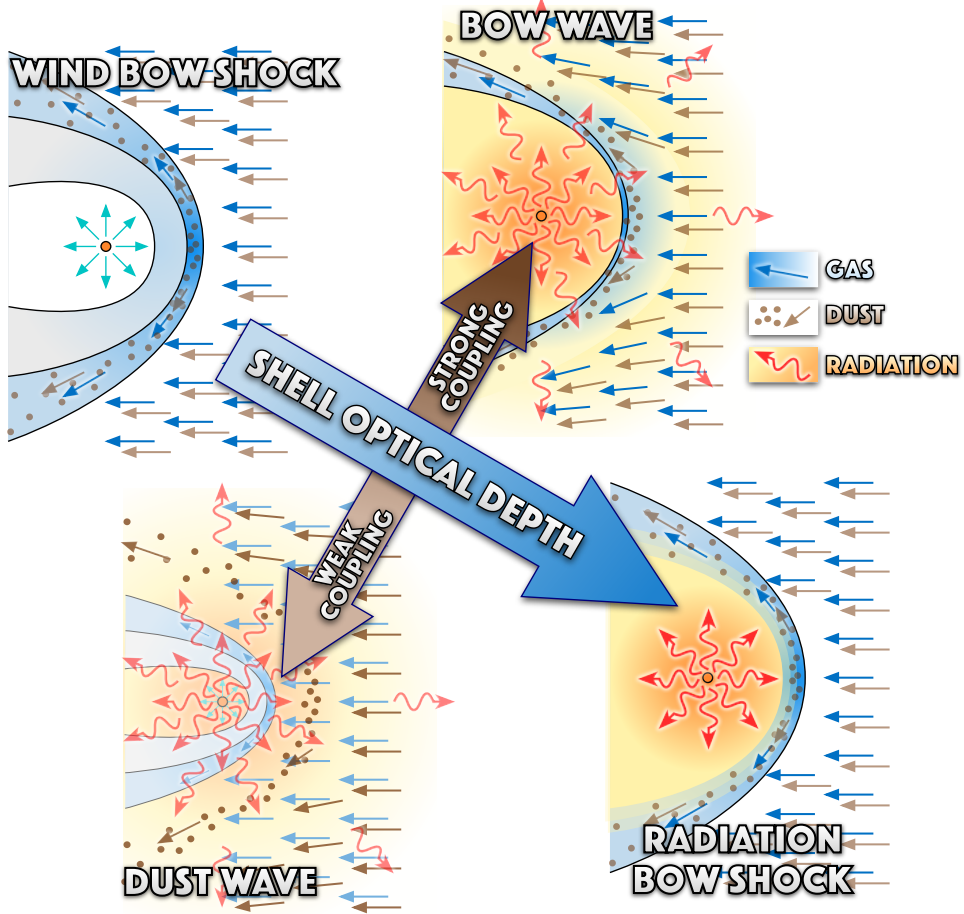


Figure 1. Bow shocks, bow waves, and dust waves

determine existence conditions for the presence of a decoupled dust wave. In § 4 we consider the additional coupling between the grains and the plasma’s magnetic field, and how this effects the existence and structure of dust waves. In § 5 we briefly discuss the application of our models to observed bows. In § 6 we summarise the conclusions of our study. A series of appendices provide additional technical information on dust physics (Appendix A), analytical models of the shape of dust waves in the drag-free limit (Appendix C), and the numerical calculation of grain trajectories (Appendix D).

2 STRONG GAS-GRAIN COUPLING

We consider the canonical case of a bow around a star of bolometric luminosity, L , with a radiatively driven wind, which is immersed in an external stream of gas and dust with density, ρ , and velocity, v . The size and shape of the bow is determined by a generalized balance of pressure (or, equivalently, momentum) between internal and external sources. We assume that the stream is supersonic and super-alfvenic, so that the external pressure is dominated by the ram pressure: ρv^2 . We first consider the case where the dust grains and gas are perfectly coupled by collisions.

Although dust grains typically constitute only a small fraction $Z_d \sim 0.01$ of the mass of the external stream, they nevertheless dominate the broad-band opacity at FUV, optical and IR wavelengths if they are present.¹ The strong coupling assumption means that all the radiative forces applied to the dust grains are directly felt by the gas also.

2.1 Bows supported by radiation and wind

The internal pressure is the sum of wind ram pressure and the effective radiation pressure that acts on the bow shell. The radiative momentum loss rate of the star is L/c and the wind momentum loss rate can be expressed as

$$\dot{M}V = \eta_w L/c, \quad (1)$$

where η_w is the momentum efficiency of the wind, which is typically < 1 (Lamers & Cassinelli 1999). If the optical depth is very large,

¹ At EUV wavelengths ($\lambda < 912 \text{ \AA}$), gas opacity dominates if the hydrogen neutral fraction is larger than ≈ 0.001 , see discussion of ionization front trapping below.



Figure 2. Bow regimes in parameter space (v, n) of the external stream for main-sequence OB stars of different masses: (a) $10 M_{\odot}$, (b) $20 M_{\odot}$, (c) $40 M_{\odot}$. In all cases, $\kappa = 600 \text{ cm}^2 \text{ g}^{-1}$ and efficient gas-grain coupling is assumed. Solid black lines of varying width show the bow size (star-apex separation, R_0), while gray shading shows the radiation bow wave regime, with lower border $\tau = \eta_w$ and upper border $\tau = 1$, where $\tau = 2\kappa\rho R_0$ is the optical depth through the bow. For bows above the red solid line, the ionization front is trapped inside the bow. Blue lines delineate different cooling regimes. Above the thin blue line ($d_{\text{cool}} = h_0$), the bow shock radiates efficiently, forming a thin shocked shell. Below the thick blue line ($d_{\text{cool}} = R_0$), the bow shock is essentially non-radiative.

then all of the stellar radiative momentum, emitted with rate L/c , is trapped by the bow shell. In the single scattering limit,² and temporarily neglecting the wind for clarity of exposition, then pressure balance at the bow apex, a distance R_0 along the symmetry axis from the star is given by

$$\frac{L}{4\pi c R_0^2} = \rho v^2, \quad (2)$$

which yields a fiducial bow shock radius in this optically thick, radiation-only limit as

$$R_* = \left(\frac{L}{4\pi c \rho v^2} \right)^{1/2}. \quad (3)$$

We now consider the opposite, optically thin limit. If the total opacity (gas plus dust) per total mass (gas plus dust) is κ (with units of $\text{cm}^2 \text{ g}^{-1}$), then the radiative acceleration is

$$a_{\text{rad}} = \frac{\kappa L}{4\pi c R^2}. \quad (4)$$

Therefore, an incoming stream with initial velocity, v_{∞} , can be brought to rest by radiation alone at a distance R_{**} where

$$\int_{R_{**}}^{\infty} a_{\text{rad}} dr = \frac{1}{2} v_{\infty}^2, \quad (5)$$

² Although it may seem inconsistent to assume single scattering in the case of high optical depths, this is defensible for the following reasons. (1) The grain albedo is not that high (typically ~ 0.5 at ultraviolet through optical wavelengths). (2) The scattered radiation field is more isotropic than the stellar field, leading to cancellation in the radiative flux. (3) Absorbed radiation is re-emitted at infrared wavelengths, where the dust opacity is very much lower.

yielding

$$R_{**} = \frac{\kappa L}{2\pi c v_{\infty}^2}. \quad (6)$$

On the other hand, we can also argue as in the optically thick case above by approximating the bow shell as a surface, and balancing stellar radiation pressure against the ram pressure of the incoming stream. The important difference when the shell is not optically thick is that only a fraction $1 - e^{-\tau}$ of the radiative momentum is absorbed by the bow, so that equation (2) is replaced with

$$\frac{L(1 - e^{-\tau})}{4\pi c R_0^2} = \rho v^2. \quad (7)$$

In the optically thin limit, $1 - e^{-\tau} \approx \tau$, so these two descriptions can be seen to agree ($R_0 \rightarrow R_{**}$) so long as

$$\tau = 2\kappa\rho R_0, \quad (8)$$

which we will assume to hold generally.

Then, defining a fiducial optical depth,

$$\tau_* = \rho\kappa R_*, \quad (9)$$

and now reinstating the stellar wind ram pressure term from equation (1), we find that the general bow radius can be written in terms of the fiducial radius as

$$R_0 = x R_*, \quad (10)$$

where x is the solution of

$$x^2 - (1 - e^{-2\tau_* x}) - \eta_w = 0. \quad (11)$$

Since this is a transcendental equation, x must be found numerically,

but we can write explicit expressions for three limiting cases:

$$x \approx \begin{cases} \text{if } \tau_* \gg 1: & (1 + \eta_w)^{1/2} \\ \text{if } \tau_*^2 \ll 1: & \tau_* + (\tau_*^2 + \eta_w)^{1/2} \approx \begin{cases} \text{if } \tau_*^2 \gg \eta_w: & 2\tau_* \\ \text{if } \tau_*^2 \ll \eta_w: & \eta_w^{1/2} \end{cases} \end{cases} \quad (12)$$

The first case, $x \approx (1 + \eta_w)^{1/2}$, corresponds to a *radiation bow shock* (RBS); the second case, $x \approx 2\tau_*$, corresponds to a *radiation bow wave* (RBW); and the third case, $x \approx \eta_w^{1/2}$, corresponds to a *wind bow shock* (WBS). The two bow shock cases are similar in that the external stream is oblivious to the presence of the star until it suddenly hits the bow shock shell, differing only in whether it is radiation or wind that is providing the internal pressure. In the intermediate bow wave case, on the other hand, the external stream is gradually decelerated by absorption of photons as it approaches the bow.³

2.2 Dependence on stellar type

We now consider the application to bow shocks around main sequence OB stars, as well as cool and hot supergiants, expressing stellar and ambient parameters in terms of typical values as follows:

$$\begin{aligned} \dot{M}_{-7} &= \dot{M}/(10^{-7} M_\odot \text{ yr}^{-1}) \\ V_3 &= V/(1000 \text{ km s}^{-1}) \\ L_4 &= L/(10^4 L_\odot) \\ v_{10} &= v_\infty/(10 \text{ km s}^{-1}) \\ n &= (\rho/\bar{m})/(1 \text{ cm}^{-3}) \\ \kappa_{600} &= \kappa/(600 \text{ cm}^2 \text{ g}^{-1}), \end{aligned}$$

where \bar{m} is the mean mass per hydrogen nucleon ($\bar{m} \approx 1.3 m_p \approx 2.17 \times 10^{-24} \text{ g}$ for solar abundances). Note that $\kappa = 600 \text{ cm}^2 \text{ g}^{-1}$ corresponds to a cross section of $\approx 10^{-21} \text{ cm}^2$ per hydrogen nucleon, which is typical for interstellar medium dust (Bertoldi & Draine 1996) at far ultraviolet wavelengths, where OB stars emit most of their radiation. In terms of these parameters, we can express the stellar wind momentum efficiency as

$$\eta_w = 0.495 \dot{M}_{-7} V_3 L_4^{-1} \quad (13)$$

and the fiducial radius and optical depth as

$$R_*/\text{pc} = 2.21 (L_4/n)^{1/2} v_{10}^{-1} \quad (14)$$

$$\tau_* = 0.0089 \kappa_{600} (L_4 n)^{1/2} v_{10}^{-1}. \quad (15)$$

In Figure 2, we show results for the bow size (apex distance, R_0) as a function of the density, n , and relative velocity, v_∞ , of the external stream, with each panel corresponding to a particular star, with parameters as shown in Table 1. To facilitate comparison with previous work, we choose stellar parameters similar to those used in the hydrodynamical simulations of Meyer et al. (2014, 2016, 2017), based on stellar evolution tracks for stars of $10 M_\odot$, $20 M_\odot$ and $40 M_\odot$ (Brott et al. 2011) and theoretical wind prescriptions (de Jager et al. 1988; Vink et al. 2000). Although the stellar parameters do evolve with time, they change relatively little during the main-sequence lifetime of several million years.⁴ The three examples

³ A shock can still form in this case, but shocked material constitutes only a small fraction of the total column density of the shell.

⁴ Note that we have recalculated the stellar wind terminal velocities, since the values given in the Meyer et al. papers are troublingly low. We have

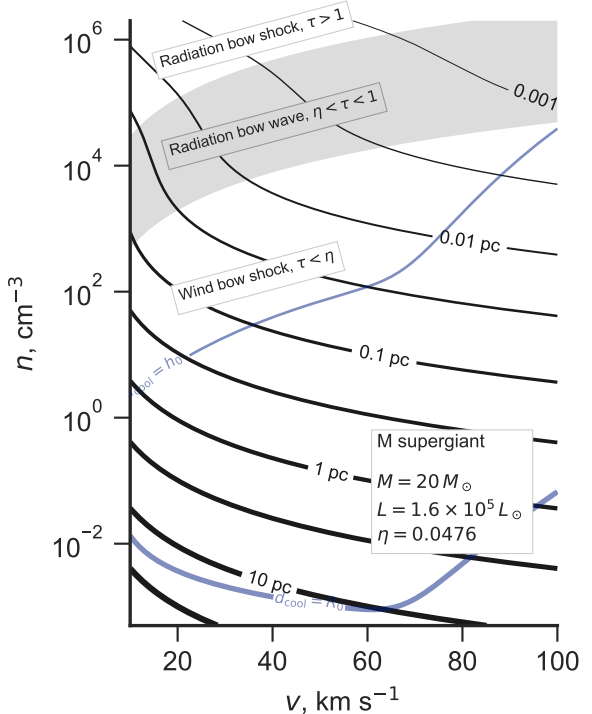


Figure 3. As Fig. 2, but for a cool M-type supergiant instead of hot main sequence stars. A smaller dust opacity is used, $\kappa = 60 \text{ cm}^2 \text{ g}^{-1}$, because of the reduced extinction efficiency at the optical/infrared wavelengths emitted by this star.

are an early B star ($10 M_\odot$), a late O star ($20 M_\odot$), and an early O star ($40 M_\odot$), which cover the range of luminosities and wind strengths expected from bow-producing hot main sequence stars. The luminosity is a steep function of stellar mass ($L \sim M^{2.5}$) and the wind mass-loss rate is a steep function of luminosity ($\dot{M} \sim L^{2.2}$), which means that the wind momentum efficiency is also a steep function of mass ($\eta_w \sim M^3$), approaching unity for early O stars, but falling to less than 1% for B stars.

It can be seen from Figure 2 that the onset of the radiation bow wave regime is very similar for the three main-sequence stars, occurring at $n > 20$ to $40 v_{10}^2$. An important difference, however, is that for the $40 M_\odot$ star, which has a powerful wind, the radiation bow wave regime only occurs for a very narrow range of densities, whereas for the $10 M_\odot$ star, with a much weaker wind, the regime is much broader, extending to $n < 10^4 v_{10}^2$. Another difference is the size scale of the bows in this regime, which is $R_0 = 0.001 \text{ pc}$ to 0.003 pc

used the prescription $V = 2.6V_{\text{esc}}$, where $V_{\text{esc}} = (2GM(1 - \Gamma_e)/R)^{1/2}$ is the photospheric escape velocity, which is appropriate for strong line-driven winds with $T_{\text{eff}} > 21000 \text{ K}$ (Lamers et al. 1995). We find velocities of 2500 km s^{-1} to 3300 km s^{-1} , which are consistent with observations and theory (Vink et al. 1999) for O stars, but at least two times higher than those cited by Meyer et al. (2014). For main-sequence B stars, wind column densities are too low to reliably measure the terminal velocity from near ultraviolet P Cygni profiles (Prinja 1989), and so the values are theory-dependent (Krtička 2014) and hence more uncertain. A further complication is the existence of a subset of OB stars with anomalously weak winds (Puls et al. 2008), which in some cases is related to the presence of strong ($\sim 1 \text{ kG}$) magnetic fields (Oskinova et al. 2011).

Table 1. Stellar parameters for example stars

	M/M_\odot	L_4	\dot{M}_{-7}	V_3	η_w	Sp. Type	T_{eff}/kK	$\lambda_{\text{eff}}/\mu\text{m}$	S_{49}	Figures
Main-sequence OB stars	10	0.63	0.0034	2.47	0.0066	B1.5 V	25.2	0.115	0.00013	2a, 8a, 9–12
	20	5.45	0.492	2.66	0.1199	O9 V	33.9	0.086	0.16	2b, 8b
	40	22.2	5.1	3.31	0.4468	O5 V	42.5	0.068	1.41	2c, 8c
Blue supergiant star	33	30.2	20.2	0.93	0.3079	B0.7 Ia	23.5	0.123	0.016	4
Red supergiant star	20	15.6	100	0.015	0.0476	M1 Ia	3.6	0.805	0	3

for the $10 M_\odot$ star if $v_\infty = 40 \text{ km s}^{-1}$, but $R_0 \approx 0.1 \text{ pc}$ for the $40 M_\odot$ star, assuming the same inflow velocity.

Figure 3 shows results for a cool M-type super-giant star with stellar parameters inspired by Betelgeuse (α Orionis), as listed in Table 1. Unlike the UV-dominated spectrum of the hot stars, this star emits predominantly in the near-infrared, where the dust extinction efficiency is lower, so we adopt a lower opacity of $60 \text{ cm}^2 \text{ g}^{-1}$. This has the effect of shifting the radiation bow wave regime to higher densities: $n = 1000$ to $30 000 v_{10}^2$ in this case.

2.3 Effects of stellar gravity

In principle, gravitational attraction from the star, of mass M , will partially counteract the radiative acceleration. This can be accounted for by replacing L with an effective luminosity

$$L_{\text{eff}} = L(1 - \Gamma_E^{-1}), \quad (16)$$

in which Γ_E is the Eddington factor:

$$\Gamma_E = \frac{\kappa L}{4\pi c GM} = 458.5 \frac{\kappa_{600} L_4}{M}, \quad (17)$$

where, in the last expression, M is measured in solar masses. For the stars in Table 1, we find $\Gamma_E \approx 30$ to 400 , so gravity can be safely ignored. The only exception is when the optical depth of the bow is very large: $\tau > \ln \Gamma_E \sim 5$, in which case gravity may be important in the outer parts of the shell (see Rodríguez-Ramírez & Raga 2016).

2.4 Ionization state of the bow shell

In this section we calculate whether the star is capable of photoionizing the entire bow shock shell, or whether the ionization front will be trapped within it. The number of hydrogen recombinations⁵ per unit time per unit area in a fully ionized shell is

$$\mathcal{R} = \alpha_B n_{\text{sh}}^2 h_{\text{sh}}, \quad (18)$$

while the advective flux of hydrogen nuclei through the shock is

$$\mathcal{A} = nv, \quad (19)$$

and the flux of hydrogen-ionizing photons ($h\nu > 13.6 \text{ eV}$) incident on the inner edge of the shell is

$$\mathcal{F} = \frac{S}{4\pi R_0^2}, \quad (20)$$

where S is the ionizing photon luminosity of the star. Any shell with $\mathcal{R} + \mathcal{A} > \mathcal{F}$ cannot be entirely photoionized by the star, and so must have trapped the ionization front.

⁵ The diffuse field is treated in the on-the-spot approximation, assuming all emitted Lyman continuum photons are immediately re-absorbed locally, so the case B recombination co-efficient, $\alpha_B = 2.6 \times 10^{-13} T_4^{-0.7} \text{ cm}^3 \text{ s}^{-1}$, is used, where $T_4 = T/10^4 \text{ K}$.

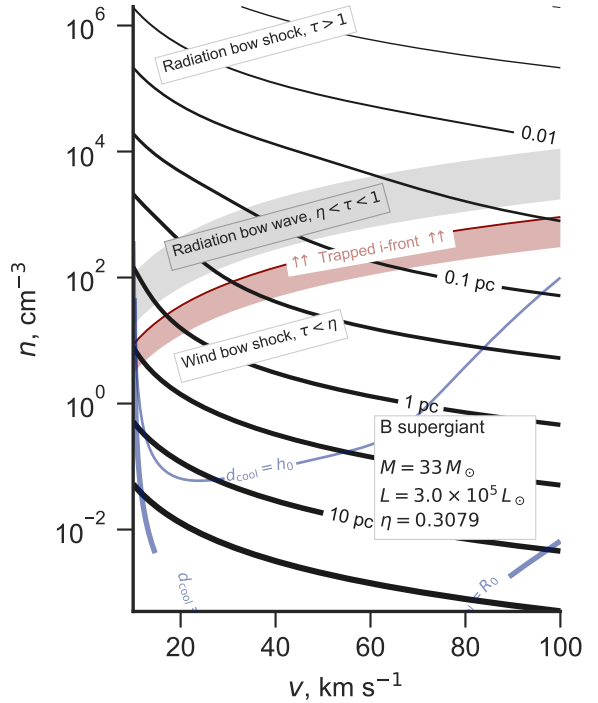


Figure 4. As Fig. 2, but for an evolved B-type supergiant instead of main sequence stars. This is similar to the early O MS star of Fig. 2c in many respects, except for the trapping of the ionization front, which occurs for much lower outer stream densities.

The ratio of advective particle flux to ionizing flux is, from equations (3), (19), (20),

$$\frac{\mathcal{A}}{\mathcal{F}} = 5.86 \times 10^{-5} \frac{x^2 L_4}{v_{10} S_{49}}, \quad (21)$$

where

$$S_{49} = S/(10^{49} \text{ s}^{-1}).$$

Numerical values of S_{49} for our three example stars are given in Table 1, taken from Figure 4 of Sternberg et al. (2003). Since $\mathcal{A} \ll \mathcal{F}$ in nearly all cases, for clarity of exposition we ignore \mathcal{A} in the following discussion, although it is included in quantitative calculations. The column density of the shocked shell can be found, for example, from equations (10) and (12) of Wilkin (1996) in the limit $v_\infty/V \rightarrow 0$ (Wilkin's parameter α) and $\theta \rightarrow 0$. This yields

$$n_{\text{sh}} h_{\text{sh}} = \frac{3}{4} n R_0. \quad (22)$$

Assuming strong cooling behind the shock,⁶ the shell density is

$$n_{\text{sh}} = M_0^2 n \quad (23)$$

where $M_0 = v_\infty/c_s$ is the isothermal Mach number of the external stream.⁷ Putting these together with equations (3) and (9), one finds that $\mathcal{R} > \mathcal{F}$ implies

$$x^3 \tau_* > \frac{4Scc_s \bar{m}^2 \kappa}{3\alpha L}. \quad (24)$$

From equation (11), it can be seen that x depends on the external stream parameters, n, v_∞ only via τ_* , and so equation (24) is a condition for τ_* , which, by using equation (15), becomes a condition on n/v_{10}^2 . In the radiation bow shock case, $x = (1 + \eta_w)^{1/2}$, and the condition can be written:

$$\text{RBS: } \frac{n}{v_{10}^2} > 2.65 \times 10^8 \frac{S_{49}^2 T_4^{3.4}}{L_4^3 (1 + \eta_w)^3}. \quad (25)$$

In the radiation bow wave case, $x = 2\tau_*$, and the condition can be written:

$$\text{RBW: } \frac{n}{v_{10}^2} > 5.36 \times 10^4 \frac{S_{49}^{1/2} T_4^{0.85}}{\kappa_{600}^{3/2} L_4^{3/2}}. \quad (26)$$

In the wind bow shock case, the result is the same as equation (25), but changing the factor $(1 + \eta_w)^3$ to η_w^3 . For the example hot stars in Table 1, and assuming $\kappa_{600} = 1, T_4 = 0.8$, the resulting density threshold is $n > (1000 \text{ to } 5000) v_{10}^2$, depending only weakly on the stellar parameters, which is shown by the red lines in Figure 2. For the $10 M_\odot$ star, this is in the radiation bow wave regime, whereas for the higher mass stars it is in the radiation bow shock regime. When the external stream is denser than this, then the outer parts of the shocked shell may be neutral instead of ionized, giving rise to a cometary compact H II region (Mac Low et al. 1991; Arthur & Hoare 2006). This is only necessarily true, however, when the star is isolated. If the star is in a cluster environment, then the contribution of other nearby massive stars to the ionizing radiation field must be considered.

Quite different results are obtained for a B-type supergiant star (see Tab. 1 and Fig. 4), which has a similar bolometric luminosity and wind strength to the $40 M_\odot$ main-sequence star, but a hundred times lower ionizing luminosity. This results in a far lower threshold for trapping the ionization front of $n > 40v_{10}^2$. The advective flux, \mathcal{A} , is relatively stronger for this star than for the main-sequence stars, but even for $v_{10} < 2$, where the effect is strongest, the change is only of order the width of the dark red line in Figure 4.

In principle, when the ionization front trapping occurs in the bow wave regime, then the curves for R_0 will be modified in the region above the red line because all of the ionizing radiation is trapped in the shell due to gas opacity, which is not included in equation (8). However, this only happens for our $10 M_\odot$ star, which has a relatively soft spectrum. Table 1 gives the peak wavelength of the stellar spectrum for this star as $\lambda_{\text{eff}} = 0.115 \mu\text{m}$, which is significantly larger than the hydrogen ionization threshold at $0.0912 \mu\text{m}$, meaning that only a small fraction of the total stellar luminosity is in the EUV band and affected by the gas opacity.

⁶ This is shown to be justified in § 2.5.

⁷ The sound speed depends on the temperature and hydrogen and helium ionization fractions, y and y_{He} as $c_s^2 = (1 + y + z_{\text{He}}y_{\text{He}})(kT/\bar{m})$, where z_{He} is the helium nucleon abundance by number relative to hydrogen and $k = 1.3806503 \times 10^{-16} \text{ erg K}^{-1}$ is Boltzmann's constant. We assume $y = 1$, $y_{\text{He}} = 0.5$, $z_{\text{He}} = 0.09$, so that $c_s = 11.4 T_4^{1/2} \text{ km s}^{-1}$.

The effect on R_0 is therefore small. For the higher mass stars, $\lambda_{\text{eff}} < 0.0912 \mu\text{m}$, so the majority of the luminosity is in the EUV band, but in these cases the ionization front trapping occurs well inside the radiation bow shock zone, where the dust optical depth is already sufficient to trap all of the radiative momentum.

2.5 Radiative cooling lengths

In this section, we calculate whether the radiative cooling is sufficiently rapid behind the bow shock to allow the formation of a thin, dense shell. Since this is mainly a concern at low densities, where cooling is least efficient, we will assume that the wind bow shock regime applies unless otherwise specified. We label quantities just outside the shock by the subscript "0", quantities just inside the shock (after thermalization, but before any radiative cooling) by the subscript "1", and quantities after the gas has cooled back to the photoionization equilibrium temperature by the subscript "2". Assuming a ratio of specific heats, $\gamma = 5/3$, the relation between the pre-shock and immediate post-shock quantities is

$$\frac{n_1}{n_0} = \frac{4M_0^2}{M_0^2 + 3} \quad (27)$$

$$\frac{T_1}{T_0} = \frac{1}{16}(5M_0^2 - 1)(1 + 3/M_0^2) \quad (28)$$

$$\frac{v_1}{v_0} = \left(\frac{n_1}{n_0}\right)^{-1}, \quad (29)$$

where $M_0 = v_0/c_s$. The cooling length of the post-shock gas can be written as

$$d_{\text{cool}} = \frac{3P_1 v_1}{2(\mathcal{L}_1 - \mathcal{G}_1)}, \quad (30)$$

where P_1 is the thermal pressure and $\mathcal{L}_1, \mathcal{G}_1$ are the volumetric radiative cooling and heating rates. For fully photoionized gas, we have $P_1 \approx 2n_1 k T_1$, $\mathcal{L}_1 = n_1^2 \Lambda(T_1)$, and $\mathcal{G}_1 = n_1^2 \Gamma(T_1)$, where $\Lambda(T)$ is the cooling coefficient, which is dominated by metal emission lines that are excited by electron collisions, and $\Gamma(T)$ is the heating coefficient, which is dominated by hydrogen photo-electrons (Osterbrock & Ferland 2006). The cooling coefficient has a maximum around 10^5 K , and for typical ISM abundances can be approximated as follows:

$$\Lambda_{\text{warm}} = 3.3 \times 10^{-24} T_4^{2.3} \text{ erg cm}^3 \text{ s}^{-1} \quad (31)$$

$$\Lambda_{\text{hot}} = 10^{-20} T_4^{-1} \text{ erg cm}^3 \text{ s}^{-1} \quad (32)$$

$$\Lambda = (\Lambda_{\text{warm}}^{-k} + \Lambda_{\text{hot}}^{-k})^{-1/k} \quad \text{with } k = 3, \quad (33)$$

which is valid in the range $0.7 < T_4 < 1000$. We approximate the heating coefficient as

$$\Gamma = 1.77 \times 10^{-24} T_4^{-1/2} \text{ erg cm}^3 \text{ s}^{-1}, \quad (34)$$

where the coefficient is chosen so as to give $\Gamma = \Lambda$ at an equilibrium temperature of $T_4 = 0.8$.

In Figure 2 we show curves calculated from equations (27) to (34), corresponding to $d_{\text{cool}} = R_0$ (thick blue line) and $d_{\text{cool}} = h_0$ (thin blue line), where h_0 is the shell thickness in the efficient cooling case. In this context, $n_0 = n$ and $n_2 = n_{\text{sh}}$, so that h_0 follows from equations (22) and (23) as

$$h_0 = \frac{3}{4} M_0^{-2} R_0. \quad (35)$$

The bends in the curves at $v \approx 50 \text{ km s}^{-1}$ are due to the maximum in the cooling coefficient $\Lambda(T)$ around 10^5 K . For bows with outer

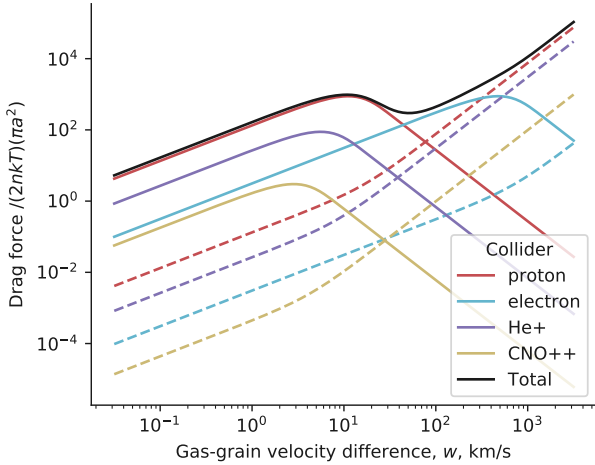


Figure 5. Contributions of different collider species to the dimensionless drag force, f_{drag}/f_* , as a function of gas–grain slip velocity, w . Solid lines show the Coulomb (electrostatic) drag, while dashed lines show the Epstein (solid-body) drag. Results are shown for dimensionless grain potential $\phi = 10$. All Coulomb forces scale with ϕ^2 , while the Epstein forces are independent of ϕ . The species labelled ‘‘CNO++’’ represents the combined effect of all metals (see footnote 10).

stream densities above the thin blue line, radiative cooling is so efficient that the bow shock can be considered isothermal, and so the shell is dense and thin (at least, in the apex region). It can be seen that the ionization front trapping always occurs at densities larger than this, which justifies the use of equation (23) in the previous section. For bows with outer stream densities below the thick blue line, cooling is unimportant and the bow shock can be considered non-radiative. In this case the shell is thicker than in the radiative case, $h_{\text{sh}}/R_0 \approx 0.2$ to 0.3 .⁸ For bows with outer stream densities between the two blue lines, cooling does occur, albeit inefficiently, so that the shell thickness is set by d_{cool} rather than h_0 .

3 IMPERFECT COUPLING BETWEEN GAS AND DUST

If the radiation field is sufficiently strong, then the collisional coupling between grains and gas will break down. In this section, we calculate the regions of star+stream parameter space where this might occur, leading to a separation of the bow into an outer dust wave and an inner, dust-free bow shock.

3.1 Drag force on grains

The drag force on a charged dust grain moving at a relative speed w through a plasma has contributions from both direct collisions and from electrostatic Coulomb interactions with ions and electrons. We use the expressions in Draine & Salpeter (1979), equations (4)–(6), considering the contributions from protons, electrons, helium

⁸ An approximate value can be found from equation (22) by substituting $n = n_0$ and $n_{\text{sh}} \approx n_1$, then using equation (27). Consideration of the slight increase in density between the shock and the contact/tangential discontinuity reduces this value by 5–10%.

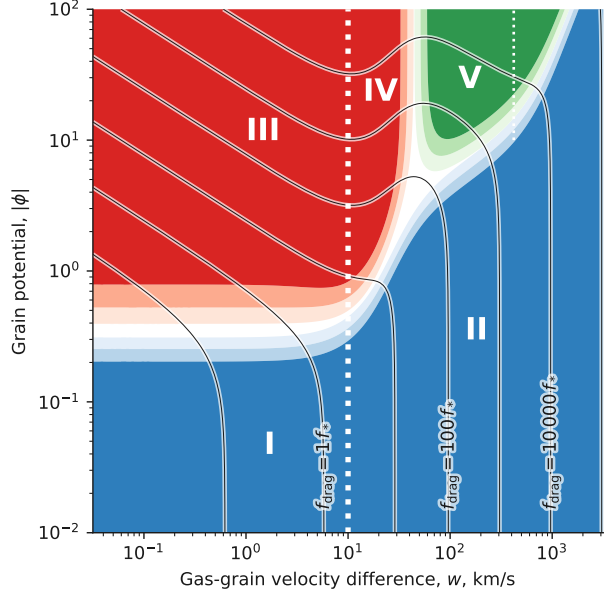


Figure 6. Regimes of gas–grain drag as a function of slip velocity and grain potential. The different regimes are indicated by bold roman numerals, as explained in Table 2. Blue shading indicates regions dominated by Epstein (solid-body) drag, whereas red and green shading indicate regions dominated by Coulomb drag due to protons and electrons, respectively. In each case, the saturated color represents a contribution > 70% of the relevant component to the total drag force, while progressively lighter shading represents the > 60% and > 50% levels. The thick white dotted line indicates the transition between the subthermal and superthermal regimes for protons, while the thin white dotted line indicates the corresponding transition for electrons. Contours show the total drag force in units of f_* (see eq. [37]) in decade intervals from 0.1 to 10^4 , as labelled. Results are shown for $T = 8000$ K and $n = 100$ cm $^{-3}$, but the differences are very slight throughout the ranges $T = 5000$ K to 15 000 K and $n = 10^{-3}$ cm $^{-3}$ to 10 6 cm $^{-3}$.

Table 2. Regimes of drag force as function of grain potential and slip speed

Regime	Approximate criteria	f_{drag}/f_*
I Epstein subsonic	$\phi^2 \ll 1$ and $w_{10} < 1$	$1.5 w_{10}$
II Epstein supersonic	$w_{10} > 1$ and $w_{10} > 5 \phi $	w_{10}^2
III Coulomb p ⁺ subthermal	$\phi^2 > 1$ and $w_{10} < 1$	$(1 + 20 \phi^2) w_{10}$
IV Coulomb p ⁺ superthermal	$\phi^2 > 1$ and $1 < w_{10} < 5$	$w_{10}^2 + 10 \phi^2/w_{10}^2$
V Coulomb e ⁻ subthermal	$\phi^2 > 20$ and $5 < w_{10} < 42$	$0.48 \phi^2 w_{10}$

ions,⁹ and metal ions.¹⁰ Results are shown in Figure 5, where dashed lines correspond to direct solid body collisions and solid lines to electrostatic interactions. The latter depend on the grain

⁹ Helium is assumed to be singly ionized, leading to only a small contribution to the drag force. For much hotter stars, such as the central stars of planetary nebulae, helium may be doubly ionized, which leads to a fourfold increase in its Coulomb drag contribution, which is significant for $w < 5$ km s $^{-1}$.

¹⁰ All metals are lumped together as a single species, assuming standard H II region gas-phase abundances. They are dominated by C and O, with minor contributions from N and Ne. The total abundance is 8.5×10^{-4} and the effective atomic weight is 15.3. All are assumed to be doubly ionized. Their largest relative contribution to the drag force is for $w < 2$ km s $^{-1}$, but is less than 1% even there.

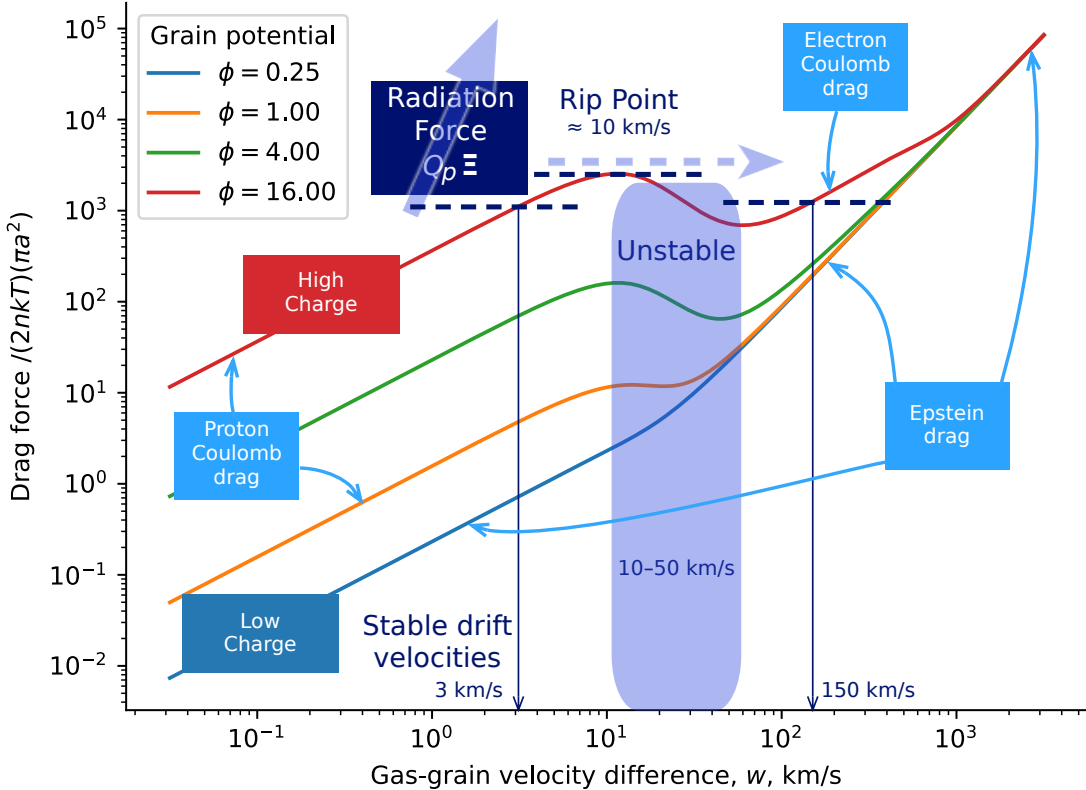


Figure 7. Dimensionless drag force, f_{drag}/f_* , as a function of gas–grain slip velocity, w , for different values of the grain potential in thermal units, ϕ . Contributions from proton and electron Coulomb (electrostatic) drag, as well as Epstein (solid-body) drag are indicated. Examples of subsonic and highly supersonic stable drift velocities are shown (thin dark blue arrows), where the drag force is in equilibrium with the radiation force (thick dark blue dashed lines), while blue shading indicates the unstable, mildly supersonic velocity regime, where no stable drift equilibrium exists. Inset graph shows ϕ as a function of the radiation parameter, $\Xi = P_{\text{rad}}/P_{\text{gas}}$ on a log–linear scale for a collection of Cloudy models (see Appendix A).

potential, which is described in dimensionless terms by ϕ , which is the electrostatic potential energy of a unit charge at the surface of a grain of charge z_d and radius a , in units of the characteristic thermal energy of a gas particle:

$$\phi = \frac{e^2 z_d}{a k T}. \quad (36)$$

The electrostatic contributions to f_{drag} are proportional to ϕ^2 (results are shown for $|\phi| = 10$), whereas the solid-body contributions are independent of ϕ . The drag force is put in dimensionless units by dividing by a characteristic force:

$$f_* = 2n k T \cdot \pi a^2, \quad (37)$$

which is approximately¹¹ the ionized gas pressure multiplied by the grain geometric cross section.

¹¹ To simplify the exposition, the gas pressure in this section is calculated assuming a fully ionized, pure hydrogen plasma, yielding $P_{\text{gas}} = 2n k T$. For typical ISM abundances, the contribution of helium and its corresponding electrons yield a correction to this of order 5%. The required modifications when a cool star interacts with a predominantly neutral gas stream are discussed later.

For grains with low electric charge, $\phi^2 \ll 1$, the drag force is dominated by direct collisions of protons with the grain (dashed red line in Fig. 5). The gas collisional mean free path is much larger than the grain size, so the drag is in the Epstein regime (Weidenschilling 1977). As the relative gas–grain slip speed, w , increases, f_{drag} first increases linearly with w reaching $f_{\text{drag}} \approx f_*$ at $w = c_s \approx 10 \text{ km s}^{-1}$, then transitions to a quadratic increase in the supersonic regime.

As $|\phi|$ increases, long-range electrostatic interactions with protons within the Debye radius (Coulomb drag) become increasingly important at subsonic relative velocities, as shown by the solid lines in Figure 5). However, the Coulomb drag has a peak when w is equal to the thermal speed of the colliders, which is $\approx 10 \text{ km s}^{-1}$ for protons, giving a maximum strength of

$$f_{\text{max}} = 0.5 (\ln \Lambda) \phi^2 f_* \approx 10 \phi^2 f_*, \quad (38)$$

where Λ is the plasma parameter (number of particles within a Debye volume), such that $\ln \Lambda = 23.267 + 1.5 \ln T_4 - 0.5 \ln n$. At highly super-thermal speeds, the Coulomb drag falls asymptotically as $f_{\text{drag}} \propto 1/w^2$. The thermal speed of electrons is higher than that of the protons by a factor of $(m_p/m_e)^{1/2}$, so that the electron Coulomb drag (solid light blue line) gives a second peak of similar strength, but at $w \approx 430 \text{ km s}^{-1}$. The behavior of f_{drag} in all these

different regimes is summarised in Table 2, in terms of ϕ and $w_{10} = w/10 \text{ km s}^{-1}$. This is further illustrated in Figure 6, where each of the drag regimes is located on the $(w, |\phi|)$ plane.

3.2 Gas–grain separation: drift and rip

In Appendix C we calculate the behaviour of an incoming stream of dust grains, subject only to the repulsive radiation force from a star. For an initial inward radial trajectory, the dust grain motion is decelerated and turned around, reaching a minimum radius R_{**} , given by equation (C2). This drag-free radiative turnaround radius, R_{**} , is smaller for higher initial inward velocities, but is independent of the density of the incoming stream. We are now in a position to see how gas–grain drag will modify this picture.

From equations (C1) and (37), we can write the radiation force acting on a grain as

$$f_{\text{rad}} = Q_p \Xi f_*, \quad (39)$$

where Q_p is the grain’s radiation pressure efficiency (see footnote 23 in Appendix C) and Ξ is the local radiation parameter, defined as the ratio of direct stellar radiation pressure to gas pressure:

$$\Xi \equiv \frac{P_{\text{rad}}}{P_{\text{gas}}} \approx \frac{L}{4\pi R^2 c (2nkT)}, \quad (40)$$

where the last expression corresponds to the optically thin limit. The grain potential ϕ is also primarily determined by Ξ , as shown in Appendix A and the inset graph of Figure 7, but with a slow dependence, which can be approximated as

$$\phi(\Xi) \approx 1.5(2.3 + \ln \Xi). \quad (41)$$

There are also slight secondary dependencies on the grain composition and stellar spectrum. The relationship given in eq. (41) is appropriate for graphite grains and for stellar effective temperatures in the range 20 kK to 30 kK. For hotter stars than this, ϕ should be multiplied by a further factor of 1.5, while for silicate grains it should be divided by 1.5.

In the outer regions of the photoionized volume around an OB star, close to the ionization front, the radiation parameter is low, with typical value $\Xi \sim 0.1$. In this regime, the negative charge current at the grain surface due to electron collisions is roughly in balance with the positive current due to the ultraviolet photoelectric effect (Weingartner & Draine 2001a), leading to a low grain potential, $|\phi| < 1$, which may be positive or negative. The low Ξ means that the radiative force is also weak: $f_{\text{rad}} \sim 0.1 f_*$ from equation (39) if $Q_p \sim 1$ at UV wavelengths, which is true for all but the smallest grains. Thus, from the equations for f_{drag} given in Table 2, the radiative force can be balanced by Epstein drag if $w_{10} \sim 0.1$, leading to a small equilibrium drift velocity, $w_{\text{drift}} < 1 \text{ km s}^{-1}$, of the grains with respect to the gas. This drift is much smaller than the inward stream velocities that we are considering ($v_\infty > 10 \text{ km s}^{-1}$), so the dust follows the gas stream at a slightly reduced velocity (< 10%), and (by mass conservation) a slightly increased density. Each grain exerts an exactly opposite force to f_{drag} upon the gas, but since the dust–gas mass ratio, Z_d , is small, this produces a negligible acceleration of the gas.

As the dusty stream approaches the star, the radiation parameter Ξ will increase, with a dependence of R^{-2} once the stream is well inside the ionization front. This increases f_{rad} (eq. [39]), but also increases the grain potential, ϕ (eq. [41]) due to the increasing dominance of grain charging by photoelectric ejection. Initially, this results in a lowering of the equilibrium drift velocity to $w_{10} \sim 0.01$ as the Coulomb drag kicks in (see Appendix A). However, at smaller

Table 3. Critical values of radiation parameter at the rip point: Ξ_\dagger

Spectrum	Grain composition	
	Graphite	Silicate
B star	1000 ± 400	350 ± 150
O star	3000 ± 500	2500 ± 500

Calculated from the Cloudy models shown in Figure A3. Uncertainties represent variations with grain size and gas density. See Appendix A for further details.

radii the slow logarithmic increase in $\phi(\Xi)$ means that the drift velocity must start increasing again to accommodate the linear increase of $f_{\text{rad}}(\Xi)$. Eventually, f_{rad} exceeds f_{max} , the maximum drag force that proton Coulomb interactions can provide (eq. [38]). This occurs at a critical value of the radiation parameter, which we denote the *rip point*: $\Xi_\dagger \sim 1000$. The variations in Ξ_\dagger with star and grain parameters, which are of order ± 0.5 dex, are listed in Table 3 and illustrated graphically in Figure A3. The radius of the rip point, R_\dagger , can be expressed in terms of R_* , the fiducial optically thick bow shock radius introduced in § 2:

$$R_\dagger = \frac{v_\infty}{c_s} \Xi_\dagger^{-1/2} R_* \approx v_{10} \Xi_\dagger^{-1/2} R_*, \quad (42)$$

where we have made use of equations (3) and (40).

What happens to the dust grain following this catastrophic breakdown of gas–grain coupling depends on the relation between the rip point radius, R_\dagger , and the drag-free radiative turnaround radius, R_{**} . If $R_\dagger > R_{**}$, then the grain’s inertia will still carry it in as far as R_{**} and the initial trajectory will be almost identical to that described in Appendix C for the drag-free case. However, after being turned around by the radiation field and pushed out past R_\dagger again, the grain will *recouple* to the gas and be dragged back for a second approach.¹² We will refer to this as an *inertia-confined dust wave* (IDW). From equations (42, 44, 46), the condition $R_\dagger > R_{**}$ corresponds to $\tau_* < (\kappa/\kappa_d)\tau_{*,\text{max}}$, which is indicated by dashed lines in the left panel of Figure 8. If, on the other hand, $R_\dagger < R_{**}$, then the tail wind provided by the gas carries the grain closer to the star than its inertia would naturally take it. When the grain finally decouples at R_\dagger it experiences a much higher unbalanced f_{rad} , which can initially accelerate it to outward velocities significantly higher than the inflow velocity if $R_\dagger \ll R_{**}$. We will refer to this case as a *drag-confined dust wave* (DDW).

3.3 Existence conditions for dust waves

In order for a separate outer dust wave to exist, it is necessary for the grains to decouple from the incoming gas stream before the stream hits the hydrodynamic bow shock caused by the stellar wind. The wind bow shock radius is $R_0 = \eta_w^{1/2} R_*$ (eq. [12]), where η_w is the wind momentum efficiency (eq. [13]). Therefore, the condition $R_\dagger > R_0$ becomes from equation (42):

$$v_{10} > v_{10,\text{min}} = (\Xi_\dagger \eta_w)^{1/2}. \quad (43)$$

For O stars, the wind efficiency is generally high ($\eta_w > 0.1$) and $\Xi_\dagger > 2000$ (Tab. 3), so that dust waves can only exist when the stream velocity is very high ($v_\infty > 150 \text{ km s}^{-1}$). For B stars, in

¹² If the initial impact parameter of the trajectory is not strictly $b = 0$, then the resultant lateral component of f_{rad} will mean that b will be much increased for the second approach.



Figure 8. Regions of stream parameter space (v, n) where dust waves may form around main-sequence OB stars of $10 M_{\odot}$, $20 M_{\odot}$ and $40 M_{\odot}$ (see Tab. 1). Figure is similar to Fig. 2, except that the velocity axis is logarithmic and extends out to 1000 km s^{-1} . Overlapping colored shapes show parameters where dust waves may be allowed in the cases of large ($a = 0.2 \mu\text{m}$) and small ($a = 0.02 \mu\text{m}$) graphite and silicate grains, as labeled in the left panel. For (v, n) outside of these shapes, dust waves cannot occur for the reasons indicated by labeled orange arrows in the center panel. Labeled dashed lines in the right panel show the correspondence between the region boundaries and each dust wave existence condition given in equations (43, 45, 46). Heavy dashed lines in the left panel show where the rip point and the drag-free turnaround radius coincide. Dust waves above these lines are drag confined, while dust waves below the lines are inertia confined.

contrast, the wind can be much weaker ($\eta_w < 0.01$) and Ξ_{\dagger} is also smaller, so that dust waves are permitted by this criterion for much lower stream velocities: ($v_{\infty} > 30 \text{ km s}^{-1}$).

However, there are other conditions that need to be satisfied in order for the dust wave to exist. For instance, the drag-free turnaround radius must also be outside the bow shock: $R_{**} > R_0$, otherwise the radiation is incapable of repelling the grain opportunistically, even once it has decoupled from the gas. From equations (3), (9), and (C2) we find

$$\frac{R_{**}}{R_*} = \frac{2\sigma_d Q_p \tau_*}{\kappa m_d}, \quad (44)$$

so, if we define a single-grain opacity as $\kappa_d = \sigma_d Q_p / m_d$, then this condition becomes

$$\tau_* > \tau_{*,\min} = 0.5 \frac{\kappa}{\kappa_d} \eta_w^{1/2}. \quad (45)$$

The average value of the factor κ/κ_d over the entire grain population must be equal to the dust–gas mass ratio, $Z_d \approx 0.01$, but the factor will vary between grains, according to their size and composition.¹³ In particular, it will be relatively larger for the largest grains ($a \approx 0.2 \mu\text{m}$), which dominate the total dust mass, and smaller for the smaller grains ($a \approx 0.02 \mu\text{m}$), which dominate the UV opacity. Given the dependence of τ_* on the stream parameters (eq. [15]), for a given stellar luminosity this condition corresponds to a minimum value for n/v_{∞}^2 .

¹³ Remember that κ is the opacity per unit mass of gas, while κ_d is the opacity per unit mass of a particular grain. In both cases, averaged over the stellar spectrum.

A third condition comes from requiring $R_{\dagger} > R_0$ in the radiation wave regime (see § 2.1), where $R_0 \approx 2\tau_* R_*$. This yields

$$\tau_* < \tau_{*,\max} = 0.5 v_{10} \Xi_{\dagger}^{-1/2}, \quad (46)$$

which, for a given stellar luminosity, corresponds to a maximum value for n/v_{∞}^4 . Thus, for a given stream velocity that satisfies equation (43), equations (45, 46) determine respectively the minimum and maximum stream density for which a dust wave can exist.

The combined effects of the three conditions are illustrated in Figure 8 for each of the three example main sequence stars from Table 1. Further restrictions on the existence of dust waves arise when the effects of magnetic fields are considered, as will be discussed in § 4 below. Note that the three conditions are restrictions solely on the formation of an *outer* dust wave, that is, outside of the wind-supported hydrodynamic bow shock. In the case of the equation (45) condition, there is a further possibility: if the gas–grain coupling (and magnetic coupling) is so weak that it is still unimportant at the higher densities found in the bow shock shell, then an inertia-confined *inner* dust wave may form inside the bow shock, even when $\tau_* < \tau_{*,\min}$. Although the same might be thought to apply to the condition of equation (43), this is not the case, since the density compression in the bow shock will reduce the radiation parameter, Ξ , which moves the rip point, R_{\dagger} , to an even smaller radius. Therefore, if radiation has not managed to decouple a grain before it passes through the shock, it is unlikely to be able to do it afterwards.

3.4 Grain trajectories along the symmetry axis

The post-decoupling behavior of the grain depends on the sign of df_{drag}/dw when $w = |v_{\infty}|$. If this derivative is positive, as is the

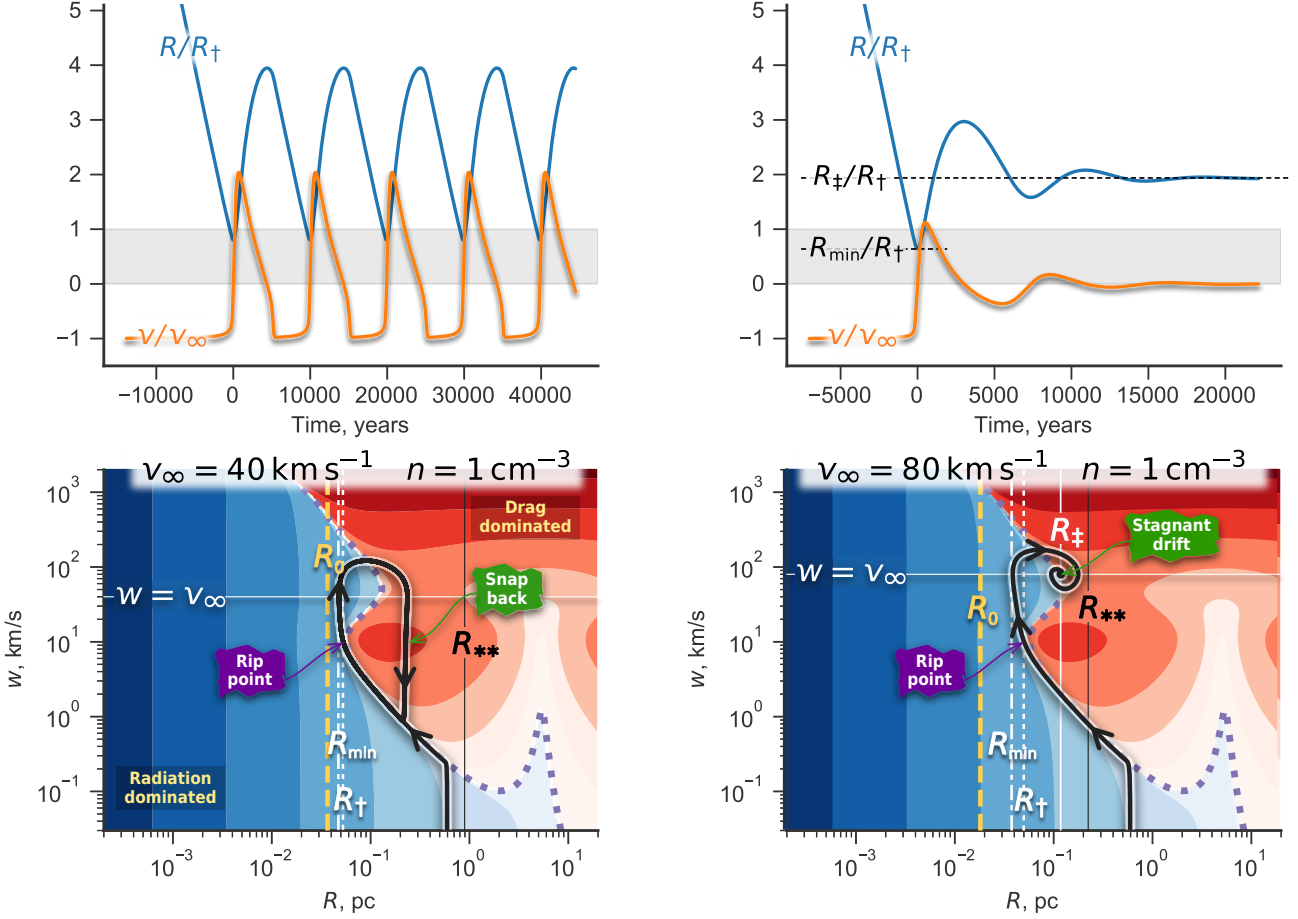


Figure 9. Trajectories of small graphite grains ($a = 0.02 \mu\text{m}$) at impact parameter $b = 0$ for two example cases (see yellow “+” symbols in left panel of Fig. 8), which differ only in the stream velocity: $v = 40 \text{ km s}^{-1}$ (left panels) and 80 km s^{-1} (right panels). In both cases, the stream density is $n = 1 \text{ cm}^{-3}$ and the central star is a $10 M_{\odot}$ main-sequence B star (see Tab. 1). Upper panels show the evolution of grain radius, R (blue curve, normalized by the rip point radius, R_{\dagger}), and grain velocity, v (orange curve, normalized by the gas stream velocity). The origin of the time axis is set to the moment of closest approach of the grain to the star: $R = R_{\min}$. Lower panels show the trajectories in phase space: position versus gas-grain relative slip velocity ($w = |v - v_{\infty}|$). Filled contours show the net force on the grain: $f_{\text{rad}} - f_{\text{drag}}$, with positive values in blue and negative values in red. The heavy dotted line shows where there is no net force: $f_{\text{rad}} = f_{\text{drag}}$. The grain trajectory (thick, solid black line with arrows) initially follows this line, but departs from it after the rip point. In the left panel, the grain enters a limit cycle between decoupling (rip) and re-coupling (snap back). In the right panel, the grain spirals in on the stagnant drift point. See text for further details.

case in drag regimes II and V (see Tab. 2 and Fig. 6), then the grain can reach a stable equilibrium drift at rest with respect to the star¹⁴ at a point R_{\ddagger} , which we call the *stagnant drift radius*. If the stream velocity is not excessively high ($v_{\infty} < 150 \text{ km s}^{-1}$ when $\phi = 4$, or $< 300 \text{ km s}^{-1}$ when $\phi = 16$), then the equilibrium f_{rad} is less than the value at the rip point, requiring a lower value of the radiation parameter: $\Xi_{\ddagger} < \Xi_{\dagger}$. The resultant stagnant drift radius is therefore outside the rip point: $R_{\ddagger} > R_{\dagger}$.

On the other hand, if $df_{\text{drag}}/dw < 0$ when $w = |v_{\infty}|$, then the equilibrium is unstable and no stagnant drift is possible. This occurs for drag regime IV, which applies when $\phi > 1$ and $10 \text{ km s}^{-1} < v_{\infty} < 50 \text{ km s}^{-1}$. There is also a second unstable regime (partially

visible in the upper-right corner of Fig. 6), which is related to the thermal peak in the electron Coulomb drag when $\phi > 30$ and $400 \text{ km s}^{-1} < v_{\infty} < 2000 \text{ km s}^{-1}$, but this is not relevant to bow shocks around OB stars.¹⁵

An example of each of these two behaviors is illustrated in Figure 9. The left panels show the case where $v_{\infty} = 40 \text{ km s}^{-1}$, which is in the unstable regime, resulting in periodic “limit-cycle” behavior (the parameters of this model correspond to the yellow “plus” symbol labeled “40” in the left panel of Fig. 8). During the grain’s first approach, it starts to follow a phase trajectory (lower left panel) along the $f_{\text{rad}} - f_{\text{drag}} = 0$ contour, corresponding to equilibrium drift, in which the grain begins to move a few km s^{-1} slower than the gas stream. Then, when it reaches the rip point

¹⁴ Again, this is only strictly true when the impact parameter is zero. However, as we show below, it is a reasonable approximation over a range of impact parameters in the case where the angle between the magnetic field direction and the stream velocity is not too large.

¹⁵ It may apply in other contexts, such as outflows from AGN, since detailed modeling of grain charging around quasars (Weingartner et al. 2006) implies that grain potentials as high as $\phi \sim 100$ can be achieved.

($R = R_{\dagger}$, $w \approx 10 \text{ km s}^{-1}$) it suddenly experiences a large unbalanced outward radiation force (blue region of phase space in Fig. 9). The grain's inward momentum carries it to the point $R_{\min} \approx 0.85R_{\dagger}$, before it is expelled at roughly twice the inflow speed. However, after moving outward, it finds itself in a drag-dominated region of phase space (red in the figure), and so recouples to the inflowing gas stream. The recoupling initiates gradually, as the grain's outward motion is slowed and it begins to move inward again, but is completed suddenly once w again falls below 10 km s^{-1} , in what we term *snap back*. The net result is that the grain has returned to exactly the same phase track that it started in on, and so repeats the cycle indefinitely.

The right panels of Figure 9 show the case where the stream velocity is doubled to $v_{\infty} = 80 \text{ km s}^{-1}$, but all other parameters remain the same. At this velocity, the equilibrium drift is stable and so the grain can achieve a stagnant drift solution, where it is stationary with respect to the star. The trajectory during the first approach is similar to the previous case, except that the overshoot of the rip point is greater, so that $R_{\min} \approx 0.65R_{\dagger}$ in this case. This is a consequence of the fact that the rip point is closer to the drag-free turnaround radius (R_{\dagger}/R_{**} is larger than in the lower velocity case), so that the grain inertia is relatively more important. A second consequence of this is that the speed of the initial expulsion is not so large, being only a little higher than the inflow velocity. The qualitative difference between the two cases emerges after the first recoupling: instead of the snap back and endless limit cycle, the grain oscillates about the stagnant drift radius with ever decreasing amplitude, so that after a few oscillation periods it has come to almost a complete rest.

3.5 Back reaction on the gas flow

So far we have ignored the effect of the drag force on the gas stream itself, but it is clear that this must become important as τ_* approaches $\tau_{*,\max}$, since that is the point where the dust wave transitions to a bow wave, in which the dust and gas are perfectly coupled. A full treatment of this problem would require solving the hydrodynamic equations simultaneously with the equations of motion of the dust grains, which is beyond the scope of this paper. Instead, we outline a heuristic approach that qualitatively captures the physics involved.

The maximum drag force experienced by a grain is at the rip point. Since the grain follows a zero-net-force phase track up until that point, this can be written with the help of equations (C1, C2) as

$$f_{\text{drag}}(R_{\dagger}) = f_{\text{rad}}(R_{\dagger}) = \frac{m_d v_{\infty}^2 R_{**}}{2R_{\dagger}^2} \quad (47)$$

The timescale of the flow can be characterized by the crossing time R_{\dagger}/v_{∞} , but the residence time of the grain at the bow apex will be several times larger than this (see previous section). On the other hand, the average drag force during this residence will be several times smaller than $f_{\text{drag}}(R_{\dagger})$ if $R_{\ddagger} > R_{\dagger}$, which is typically the case. We therefore parameterize our ignorance via a dimensionless factor, α , which we expect to be of order unity, and write the total impulse imparted to the grain by drag as

$$J_{\text{drag}} \equiv \int f_{\text{drag}} dt \approx \alpha f_{\text{drag}}(R_{\dagger}) \frac{R_{\dagger}}{v_{\infty}} = \frac{1}{2} \alpha m_d v_{\infty} \frac{R_{**}}{R_{\dagger}}. \quad (48)$$

By Newton's Third Law, an equal and opposite impulse is imparted to the gas, which will act to decelerate the gas stream as it decouples from the grains. Realistically, J_{drag} should be summed over the grain size distribution, but for simplicity we assume that all grains are identical, so that the mass of gas that accompanies each

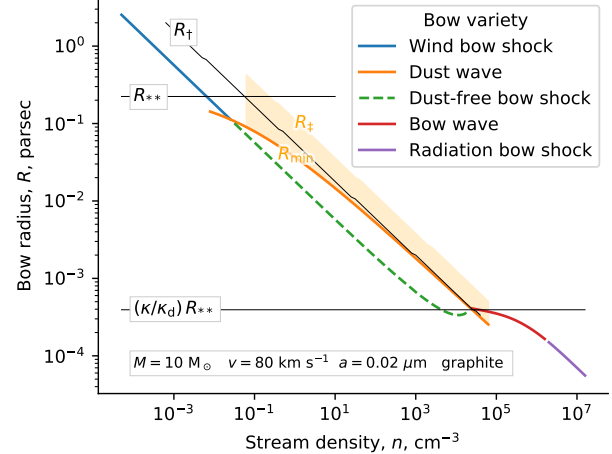


Figure 10. Bow radius as a function of stream density for a stream of initial velocity 80 km s^{-1} , which interacts with a $10 M_{\odot}$ main-sequence B star. This corresponds to a vertical slice through the left panel of Fig. 8. At low densities, the hydrodynamic bow shock (blue line) is larger than the drag-free turnaround radius for small carbon grains, meaning that a grain's inertia carries it into the bow shock along with the gas, even though the gas–grain coupling is not particularly strong. At densities above about 0.05 cm^{-3} , however, this is no longer true and a separate dust wave forms outside of the hydrodynamic bow shock, which is now dust-free (green dashed line). The grains in the dust wave will occupy a range of radii (pale orange shading) between R_{\min} (solid orange line) and R_{\ddagger} , the stagnant drift radius. At densities above about 1000 cm^{-3} , the gas stream starts to feel the effect of passing through the dust wave, and above $3 \times 10^4 \text{ cm}^{-3}$, the dust wave and bow shock merge to form a radiative bow wave (red line), which becomes an optically thick radiative bow shock (purple line) above 10^6 cm^{-3} .

grain is given by

$$m_{\text{gas}} = \frac{m_d}{Z_d} = m_d \frac{\kappa_d}{\kappa}. \quad (49)$$

If the gas remains supersonic after decoupling, then thermal pressure can be ignored and the gas will suffer a change in momentum equal to J_{drag} , so that its velocity is reduced by $\Delta v = J_{\text{drag}}/m_{\text{gas}}$, which by equations (42, 44, 46, 48, 49) is

$$\Delta v = \frac{1}{2} \alpha \frac{\tau_*}{\tau_{*,\max}} v_{\infty}. \quad (50)$$

This deceleration reduces the gas stream's ram pressure before it interacts with the central star's stellar wind. The radius of the dust-free bow shock formed by this interaction is therefore increased by a factor $(1 - \Delta v/v_{\infty})^{-1}$ with respect to the case calculated in § 2.1, yielding

$$R_{\text{dfbs}} \approx \frac{\eta_w^{1/2} R_*}{1 - \frac{1}{2} \alpha \tau_*/\tau_{*,\max}}. \quad (51)$$

An example is illustrated in Figure 10, where the dust-free bow shock radius is shown by the green dashed line as a function of stream density, n . This is calculated for fixed stream velocity and grain and star properties, so that $\tau_* \propto n^{1/2}$ (eq. [15]). In order for R_{dfbs} to match the dust-wave and bow-wave radii at the point where they cross at $\tau_* = \tau_{*,\max}$, we find $\alpha \approx 1.5$ is required. It can be seen that the gas deceleration is negligible over most of the density range for which a separate dust wave arises. Only for $n > 10^3 \text{ cm}^{-3}$ does R_{dfbs} begin to curve up from the general $n^{-1/2}$ trend, becoming

essentially flat at a value $R_{\text{dfbs}} \approx (\kappa/\kappa_d)R_{**}$ until full-coupling is established at $n > 3 \times 10^4 \text{ cm}^{-3}$. Note, however, that the treatment described here is very approximate: it does not take into account the shock that will form once J_{drag} reaches an appreciable fraction of $m_{\text{gas}}v_{\infty}$ and, additionally, it includes a factor, α , whose value has not been rigorously justified. More detailed modeling is required to fully understand the bow behavior in this transition regime.

4 MAGNETIC COUPLING OF GRAINS

An important effect that we have not considered up to now is the Lorentz force on charged grains due to the plasma's magnetic field:

$$\mathbf{f}_B = \frac{z_d e}{c} \mathbf{w} \times \mathbf{B}. \quad (52)$$

The direction of the force is perpendicular both to the magnetic field, \mathbf{B} , and to the relative velocity, \mathbf{w} , of the grain with respect to the plasma. If \mathbf{w} and \mathbf{B} (as seen by the grain) are changing slowly, compared with the gyrofrequency, $\omega_B = z_d e B / m_d c$, then the grain motion perpendicular to \mathbf{B} is constrained to be a circle of radius equal to the Larmor radius:

$$r_B = \frac{m_d c w_{\perp}}{|z_d| e B}, \quad (53)$$

where $B = |\mathbf{B}|$ and w_{\perp} is the perpendicular component of \mathbf{w} . The component of \mathbf{w} parallel to \mathbf{B} is unaffected by f_B , so the resultant trajectory is helical.

The relative importance of the magnetic field can be characterized by the ratio of the Larmor radius to the minimum radius, R_{\min} , reached by the grain in the dust wave (see § 3.4), where $R_{\min} \approx R_{\dagger}$ for drag-confined dust waves (DDW), or $R_{\min} \approx R_{**}$ for inertia-confined dust waves (IDW). We write the field strength in terms of the Alfvén speed,

$$v_A = \frac{B}{(4\pi\rho_{\text{gas}})^{1/2}} = 1.9 \frac{B}{\mu G} n^{-1/2} \text{ km s}^{-1}, \quad (54)$$

and the grain charge $z_d e$ in terms of the potential ϕ (eq. [36]) to obtain

$$\text{DDW: } \frac{r_B}{R_{\min}} = \frac{r_B}{R_{\dagger}} = 0.0140 a_{\mu\text{m}}^2 \frac{w_{\perp}}{v_A} \left(\frac{\Xi_{\dagger}}{L_4 T_4} \right)^{1/2} \frac{\rho_d}{\phi_{\dagger}} \quad (55)$$

and

$$\text{IDW: } \frac{r_B}{R_{\min}} = \frac{r_B}{R_{**}} = 0.0544 a_{\mu\text{m}}^3 \frac{w_{\perp}}{v_A} \frac{v_{10}^2}{n^{1/2}} \frac{1}{L_4 T_4} \frac{\rho_d^2}{Q_p \phi_{**}}, \quad (56)$$

where $a_{\mu\text{m}} = a/1 \mu\text{m}$, ρ_d is the grain material density in g cm^{-3} , and we have made use of equations (14, 42, C2).

If $r_B/R_{\min} \ll 1$, then the grains are so strongly coupled to the field that they can be treated in the guiding-center approximation, in which the trajectory is decomposed into a tight circular gyromotion around the field lines, plus a sliding of the guiding center along the field lines, which is governed by the radiation and drag forces (the slow $\mathbf{f} \times \mathbf{B}$ drift across the field lines is negligible in this case, see App. C3). In the opposite limit, $r_B/R_{\min} \gg 1$, magnetic coupling is so weak that the non-magnetic results of § 3 are scarcely modified. Assuming $w_{\perp} \sim v_{\infty}$ and adopting a threshold of $r_B/R_{\min} < 0.1$, equations (55, 56) can be transformed into conditions on the stream velocity (in km s^{-1}) where tight magnetic coupling will apply:

$$v_{\infty} < v_{\text{tight}} \approx \begin{cases} \text{drag-confined: } & 0.8 a_{\mu\text{m}}^{-2} v_A L_4^{1/2} \\ \text{inertia-confined: } & 6 a_{\mu\text{m}}^{-1} v_A^{1/3} n^{1/6} L_4^{1/3} \end{cases}, \quad (57)$$

where we have substituted typical values of the minor parameters

¹⁶ The most significant systematic variation in v_{tight} from these suppressed parameters is due to grain composition, yielding slightly higher values for graphite than for silicate (± 0.15 dex).

¹⁷ The reason for using a higher density is to decrease the amplitude of the radial oscillations of the trajectories, which allows the dust wave structure to be more clearly perceived in the figures.

4.1 Grain trajectories with tight magnetic coupling

We can now investigate how the results of the previous sections are modified by magnetic fields in the tight coupling limit. For simplicity, we assume a uniform field in the incoming stream, with field lines oriented at an angle θ_B to the velocity vector that defines the bow axis. We also assume a super-alfvénic stream, $v_{\infty} > v_A$, so that the radius, R_0 , of the wind bow shock is unaffected by the magnetic field, and additionally assume $\tau_* \ll \tau_{*,\text{max}}$, so that the back-reaction of the grain drag on the plasma is negligible (see previous section) and B remains uniform in magnitude and direction in the dust wave region, outside of the bow shock.

In Appendix C3, we derive analytic and semi-analytic results in the limit of zero gas-grain drag, which is appropriate for inertia-confined dust waves. We find very different structures, depending on the orientation of the field. For a parallel field (Fig. C2), the apex of the dust wave occurs at the same point, R_{**} , as in the non-magnetic case, but the shape of the dust wave wings is more closed, being hemispherical rather than parabolic in shape. For a perpendicular field (Fig. C3), on the other hand, grains in the apex region are dragged very close to the star and no dust wave forms there. A dust wave can form in the wings, with impact parameter $> R_{**}$, which is roughly parabolic in shape, but more swept-back than in the non-magnetic case. Whether such a dust wave will exist in practice depends critically on the size and shape of the MHD wind-supported bow shock.

In Figures 11 and 12 we show example results for drag-confined dust waves, which are calculated by numerically integrating the grain's equation of motion, as described in Appendix D. Apart from the inclusion of the magnetic field, the model parameters are the same as used in Figure 9, with the exception that the stream density is increased to 10 cm^{-3} .¹⁷ This time, we use quasi-parallel ($\theta_B = 10^\circ$) and quasi-perpendicular ($\theta_B = 75^\circ$) field orientations. The quasi-parallel field is most similar to the non-magnetic case, and the models shown in the two upper panels of Figure 11 closely mirror the cases shown in Figure 9, with a limit cycle behavior when $v_{\infty} = 40 \text{ km s}^{-1}$ and stagnant drift when $v_{\infty} = 80 \text{ km s}^{-1}$.

The principle difference from the 1-D axial trajectories discussed in § 3.4 is that the small 10° misalignment of \mathbf{B} from the incident stream direction causes a slow sideways migration, which puts a finite limit on the time a grain can reside in front of the star. This can be appreciated more clearly in Figure 12, which shows the grain position and velocity along a sample streamline with initial impact parameter $b = -0.4R_{\dagger}$ for the two quasi-parallel models. In panel a, corresponding to $v_{\infty} = 40 \text{ km s}^{-1}$, we see the same

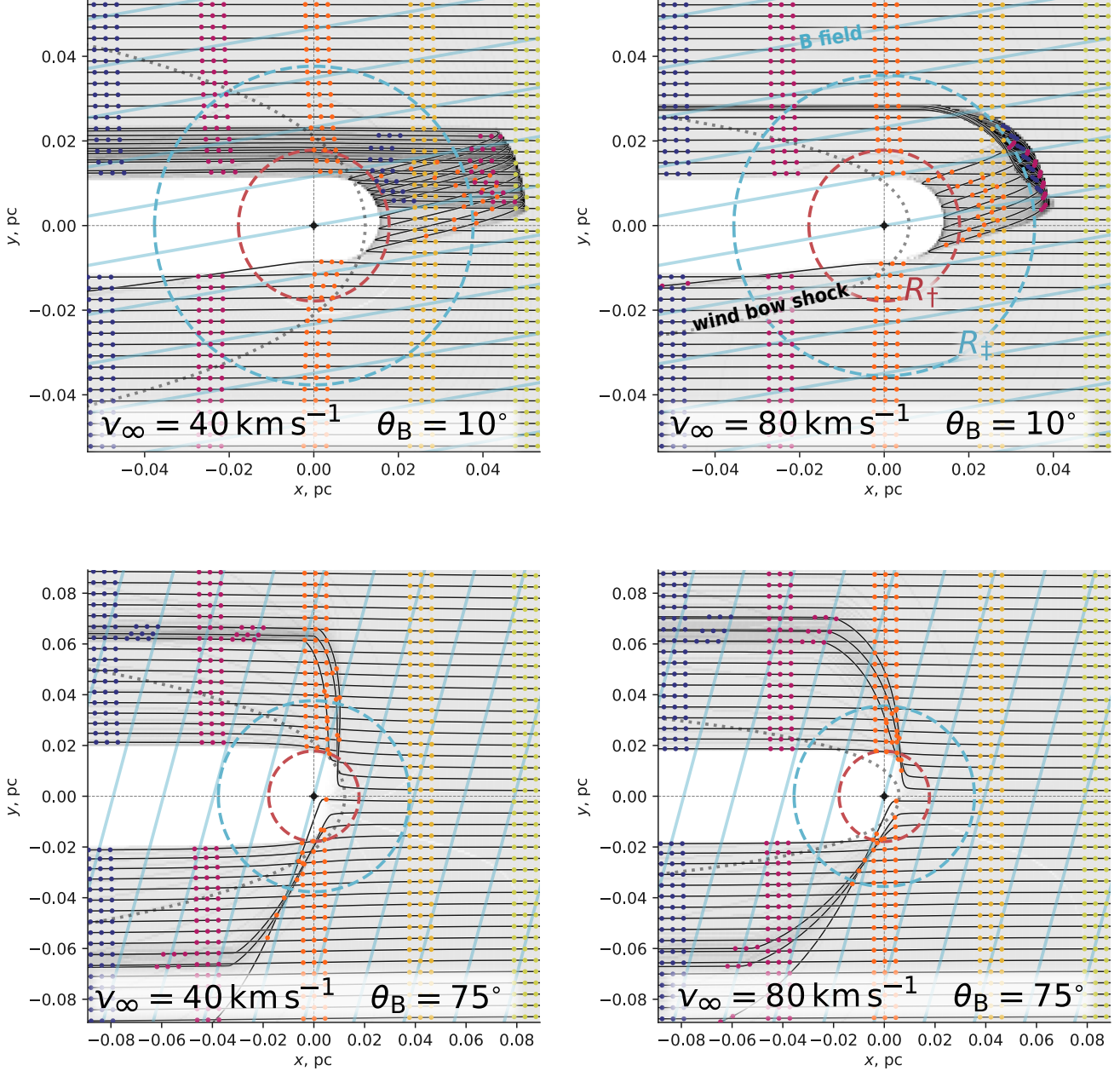


Figure 11. Drag-confined dust waves with tight magnetic coupling. Upper panels show a quasi-parallel field, $\theta_B = 10^\circ$, while lower panels show a quasi-perpendicular field, $\theta_B = 75^\circ$. Left panels show an incident stream velocity of $v_\infty = 40 \text{ km s}^{-1}$, while right panels show $v_\infty = 80 \text{ km s}^{-1}$. In all cases, the stream density is $n = 10 \text{ cm}^{-3}$ and the calculations are performed for small graphite grains, $a = 0.02 \mu\text{m}$, and the $10 M_\odot$ main-sequence B star. Continuous black lines show grain trajectories, with triplets of colored symbols indicating the progress of individual cohorts, which entered from the right edge at a particular time. Continuous blue lines show the magnetic field, which flows from right to left along with the incident stream. The radius of the rip point, R_\dagger , and the stagnant drift point, R_\ddagger , are shown respectively by red and blue dashed lines. The approximate shape of the wind-supported bow shock is shown by the dotted gray line. The calculations are no longer valid after trajectories cross this surface.

rip-and-snap-back cycle of de-coupling and re-coupling that was discussed previously, but only two periods of the cycle are completed before the grain's lateral migration takes it as far as $y \approx +R_\dagger$, at which point nothing can stop the gas stream from dragging it past the star and away. All told, the grain remains in the apex region for about $1/\sin \theta_B$ times longer than the crossing time, R_\dagger/v_∞ .

In panel b, corresponding to $v_\infty = 80 \text{ km s}^{-1}$, the grain settles for a while around the stagnant drift radius, R_\ddagger , after the initial rip and turn around. Again, it slowly migrates sideways, and eventually recouples to the incident stream, but this time after reaching $y \approx +R_\ddagger$. The grain residence time in the apex region, measured in crossing times, is slightly longer than in panel a, but is of the same order. In

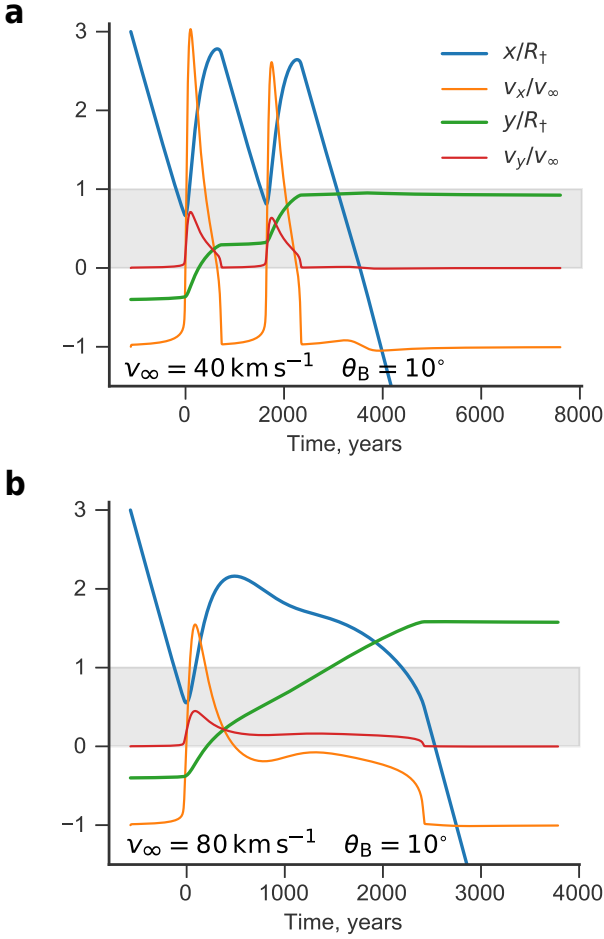


Figure 12. Sample grain trajectories for drag-confined dust waves with tight magnetic coupling and a quasi-parallel field orientation. These are the same models as in the upper row of Fig. 11. (a) Incident stream velocity of $v_\infty = 40 \text{ km s}^{-1}$, showing quasi-limit-cycle behavior (0 to 4000 years). (b) Incident stream velocity of $v_\infty = 80 \text{ km s}^{-1}$, showing quasi-stagnation behavior (500 to 2000 years). In both cases, the streamline with initial impact parameter $y = -0.4R_\dagger$ is shown.

both these cases, a second, exterior dense shell is formed in addition to the hemispherical one produced by the initial turn around inside R_\dagger . In the limit-cycle case, it forms at the snap-back point, while in the stagnant-drift case, it forms at R_\dagger and is significantly denser than the interior shell (upper right panel of Fig. 11).

The assumptions behind these models break down when the grain trajectory intersects the outer shock of the dust-free wind-supported bow shock. The increased gas density in the bow shock shell will reduce Ξ , which is likely to cause gas-grain recoupling in the case of drag-confined dust waves (see also discussion in the final paragraph of § 3.3). However, detailed modeling of this requires magnetohydrodynamical simulations, which are beyond the scope of this paper. In Figure 11 we show in gray dotted lines the Wilkinoid surface (Wilkin 1996), which is an approximation to the shape of the inner bow shock, see Paper I. It can be seen that the majority of dust streamlines do not cross this surface until well into the wings of the bow, so that a separate exterior dust wave can exist for this quasi-parallel magnetic field orientation.

This is no longer the case for the quasi-perpendicular field

orientation, as illustrated in the lower panels of Figure 11, where the behavior is similar to the perpendicular inertia-confined case studied in Appendix C3.2. Although the grains decouple from the gas inside the rip point, for small impact parameters the magnetic geometry does not allow the radiation field to expel them until they are much nearer to the star. Since the inner wind-supported bow shock radius is only a few times smaller than R_\dagger , it is possible that they will pass through the shock surface and re-couple before expulsion can occur. For the 40 km s^{-1} model (lower left panel), all of the streamlines with impact parameters $|b| < R_\dagger$ intersect the Wilkinoid surface before they are deflected, and so no separate dust wave would form in this case. For the 80 km s^{-1} model (lower left panel), some of the streamlines (mainly those with $b > 0$) do manage to avoid crossing the bow shock surface, so it is possible that a dust wave may still form, although it would only be on one side of the axis.

5 DISCUSSION

In order to provide an empirical anchor to our theoretical calculations, we now consider how the parameters of our models might be determined from observations. The parameter space diagrams, such as Figures 2 and 8, are not particularly useful in this regard, since in many cases the ambient density and relative stellar velocity are not directly measured. Instead, we aim to construct diagnostics based on the most common observations, which are of the infrared dust emission. Key questions that we wish to address include

1. Can we distinguish observationally between radiation support (bow waves and dust waves) and wind support (bow shocks)?
2. Are there any clear examples of sources with radiation-supported bows?
3. In the case of wind support, can we reliably determine mass loss rates from mid-infrared observations?

5.1 Energy trapping versus momentum trapping

A fundamental parameter is the optical depth, τ , of the bow shell to UV radiation, which determines what fraction of the stellar photon momentum is available to support the shell (see § 2.1). But the same photons also heat the dust grains in the bow, which re-radiate that energy predominantly at mid-infrared wavelengths (roughly $10 \mu\text{m}$ to $100 \mu\text{m}$) with luminosity L_{IR} . Assuming that Ly α and mechanical heating of the dust shell is negligible (see § B1) and that the emitting shell subtends a solid angle Ω , as seen from the star, then the optical depth can be estimated as

$$\tau = -\ln\left(1 - \frac{4\pi}{\Omega} \frac{L_{\text{IR}}}{L_*}\right) \approx \frac{2L_{\text{IR}}}{L_*}, \quad (58)$$

where the last approximate equality holds if $\tau \ll 1$ and the shell emission covers one hemisphere.¹⁸

A second important parameter is the thermal plus magnetic pressure in the shocked shell, which is doubly useful since in a steady state it is equal to *both* the internal supporting pressure (wind ram pressure plus absorbed stellar radiation) *and* the external confining pressure (ram pressure of ambient stream). The shell pressure is not given directly by the observations, but can be determined by the following three steps:

¹⁸ The τ of § 2.1 is not exactly the same as the τ of equation (58), but is larger by a factor of $Q_P/Q_{\text{abs}} = 1 + \varpi(1-g)/(1-\varpi)$, where ϖ is the grain albedo and g the scattering asymmetry (see App. C).

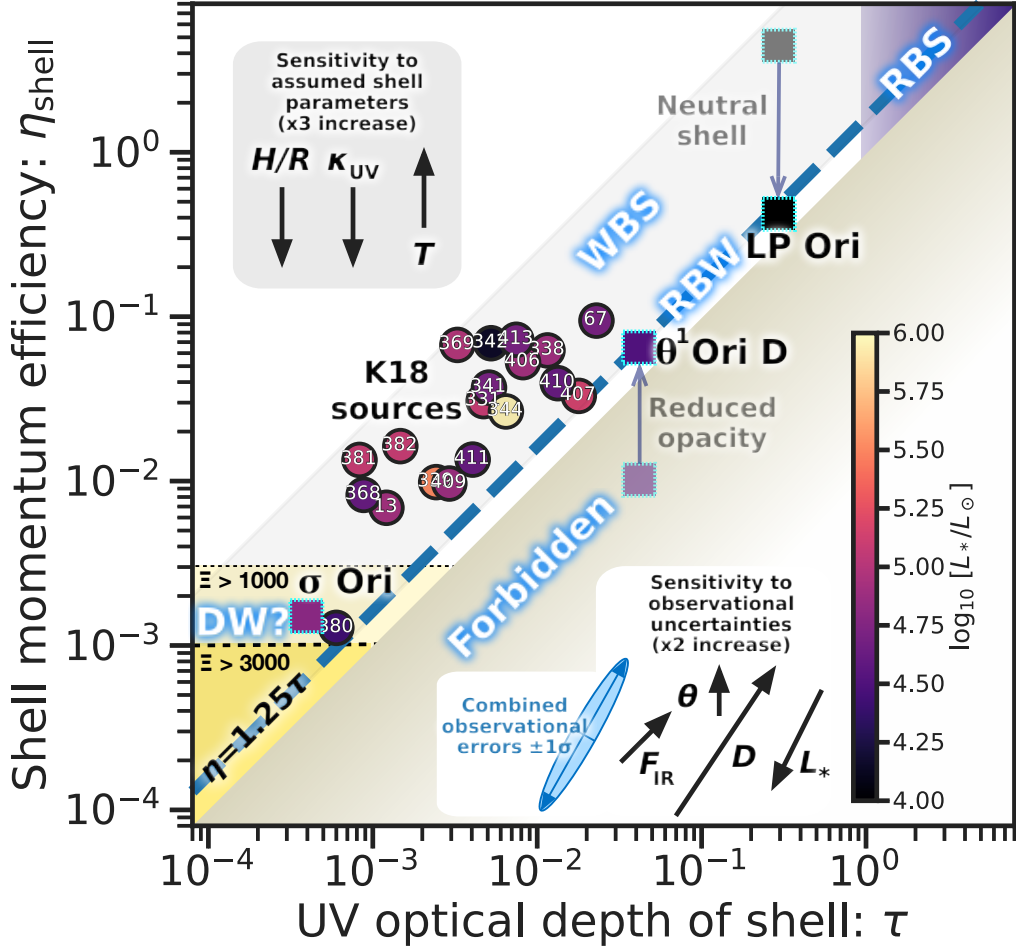


Figure 13. Observational diagnostic diagram for bow shocks. The shell optical depth τ (x axis) and momentum efficiency η_{sh} (y axis) can be estimated from observations of the bolometric stellar luminosity, infrared shell luminosity, and shell radius, as described in the text. Results are shown for the 20 sources (circle symbols) from Kobulnicky et al. (2018) plus three further sources (square symbols), where we have obtained the measurements ourselves (see Tab. 4). The color of each symbol indicates the stellar luminosity (dark to light) as indicated by the scale bar. The shell pressure is determined assuming a gas temperature $T = 10^4$ K, an absorption opacity $\kappa = 600 \text{ cm}^2 \text{ g}^{-1}$, and a thickness-to-radius ratio $H/R = 0.25$. The sensitivity of the results to a factor-of-three change in each parameter is shown in the upper inset box. Exceptions are the two Orion Nebula sources, θ^1 Ori D and LP Ori, where the small dim squares show the results of assuming the standard shell parameters, while the large squares show the results of modifications according to the peculiar circumstances of each object, as described in the text. The lower inset box shows the sensitivity of the results to a factor-of-two uncertainty in each observed quantity: distance to source D ; stellar luminosity L_* ; shell infrared flux F_{IR} ; shell angular size θ . Lines and shading indicate different theoretical bow regimes (see §§ 2 and 3). The dashed blue diagonal line corresponds to radiation-supported bows, while the upper left region corresponds to wind-supported bows. The upper right corner (purple) corresponds to optically thick bow shocks, while the lower left corner (yellow) is the region where grain-gas separation *may* occur, leading to a potential dust wave. However, the existence of a dust wave in this region is not automatic, since it only includes one of the four necessary conditions (§ 3.3 and § 4.1). The lower-right region is strictly forbidden, except in case of violation of the assumption that dust heating be dominated by stellar radiation.

P1. The shell mass column (g cm^{-2}) can be estimated from the optical depth by assuming an effective UV opacity: $\Sigma_{\text{sh}} = \tau / \kappa$

P2. The shell density (g cm^{-3}) can be found from the mass column if the shell thickness is known: $\rho_{\text{sh}} = \Sigma / h_{\text{sh}}$. In the absence of other information, a fixed fraction of the shell radius can be used.

In particular, we normalize by a typical value of one quarter¹⁹ the star-apex distance: $h_{1/4} = h_{\text{sh}} / (0.25R_0)$.

P3. Finally, the pressure (dyne cm^{-2}) follows by assuming values for the sound speed and Alfvén speed: $P_{\text{sh}} = \rho_{\text{sh}}(c_s^2 + \frac{1}{2}v_A^2)$.

It is natural to normalize this pressure to the stellar radiation pressure

¹⁹ This corresponds to a Mach number $M_0 = \sqrt{3}$ if the stream shock is radiative, or $M_0 \gg 1$ if non-radiative (see § 2.5). Further discussion is given in Appendix E

Table 4. Key observational parameters for star/bow systems

Star	L_*/L_\odot	L_{IR}/L_\odot	R_0/pc
θ^1 Ori D	2.95×10^4	620	0.003
LP Ori	1600	240	0.01
σ Ori	6×10^4	15	0.12
K18 Sources	1.4×10^4 to 8.7×10^5	8 to 2800	0.02 to 1.35

at the shell, so we define a shell momentum efficiency

$$\eta_{\text{sh}} \equiv \frac{P_{\text{sh}}}{P_{\text{rad}}} = \frac{4\pi R_0^2 (c_s^2 + \frac{1}{2}v_A^2) \tau}{L_* \kappa h_{\text{sh}}} \approx 245 \frac{R_{\text{pc}} T_4 \tau}{L_4 \kappa_{600} h_{1/4}}, \quad (59)$$

where in the last step we have assumed ionized gas with negligible magnetic support ($v_A \ll c_s$) and written the stellar luminosity and shell parameters in terms of typical values, as in § 2.2. Note that the shell momentum efficiency is simply the reciprocal of the radiation parameter of equation (40): $\eta_{\text{sh}} = \Xi_{\text{sh}}^{-1}$, which provides yet a third use for η_{sh} , since Ξ is paramount in determining whether the grains and gas remain well-coupled (see § 3.3).

5.2 The $\eta_{\text{sh}}-\tau$ diagnostic diagram

In Figure 13 we show the resultant diagnostic diagram: η_{sh} versus τ . The horizontal axis shows the fraction of the stellar radiative energy that is reprocessed by the bow shell, while the vertical axis shows the fraction of stellar radiative *momentum* that is imparted to the shell, either directly by absorption, or indirectly by the stellar wind (which is itself radiatively driven). Radiatively supported bows (DW, RBW, or RBS, or cases) should lie on the diagonal line $\eta_{\text{sh}} = (Q_P/Q_{\text{abs}})\tau \approx 1.25\tau$, where we have used the ratio of grain radiation pressure efficiency to absorption efficiency found in the FUV band for the dust mixture shown in Figure A1. Wind-supported bows should lie above this line and no bows should lie below the $\eta_{\text{sh}} = \tau$ line, since Q_P cannot be smaller than Q_{abs} .

We have calculated η_{sh} and τ using the above-described methods for the 20 mid-infrared sources studied by Kobulnicky et al. (2018) (K18) and plotted them on our diagnostic diagram. Details of our treatment of this observational material are provided in Appendix E. In order to expand the range of physical conditions, we have included three additional sources (data in Table 4): bows around θ^1 Ori D (Smith et al. 2005) and LP Ori (O'Dell 2001) in the Orion Nebula, which show larger optical depths, plus the inner bow around σ Ori, which illuminates the Horsehead Nebula and has previously been claimed to be a dust wave (Ochsendorf et al. 2014a; Ochsendorf & Tielens 2015). Details of the observations of these additional sources will be published elsewhere.

5.2.1 Random uncertainties due to observational errors

The fundamental observational quantities that go into determining τ and η_{sh} for each source are distance, D ; stellar luminosity, L_* ; total infrared flux, F_{IR} ; and bow angular apex distance, θ . From these, the shell radius and infrared luminosity are found as $R_0 = \theta D$ and $L_{\text{IR}} = 4\pi D^2 F_{\text{IR}}$. Rather than clutter the diagram with error bars, we instead show the sensitivity to observational errors in the lower-right box, where each arrow corresponds to a factor of two increase (0.3 dex) in each quantity: D , L_* , F_{IR} , and θ . In § E1 we estimate the uncertainty in each observational quantity for the K18 sources. We then combine these in § E2 to find the $\pm 1\sigma$ error ellipse, shown in blue in the figure. It can be seen that observational

uncertainties in τ and η_{sh} are highly correlated: the dispersion is 0.7 dex in the product $\eta_{\text{sh}}\tau$ but only 0.16 dex in the ratio η_{sh}/τ , with stellar luminosity errors dominating in both cases. Observational uncertainties are therefore relatively unimportant in determining whether a given source is wind-driven or radiation-driven, which depends only on η_{sh}/τ . On the other hand, they do significantly effect the question of whether a source has a sufficiently high radiation parameter Ξ to possibly be a dust wave.

5.2.2 Systematic uncertainties due to assumed shell parameters

A further source of uncertainty arises from the parameters of the shocked shell that are assumed in steps P1–P3, namely the relative shell thickness, h_{sh}/R_0 , the ultraviolet grain opacity per mass of gas, κ , and the shell temperature, T . These parameters effect only η_{sh} , not τ , with a sensitivity shown by arrows in the upper left box of Figure 13.

Shell thickness We do not expect a great deal of variation in the shell thickness, except for in the case of fast runaway stars ($v > 100 \text{ km s}^{-1}$), for which the shell may be dramatically thinner if the post-shock cooling is sufficiently rapid ($h/R_0 \sim M_0^{-2}$). For ambient densities less than about 10 cm^{-3} , the minimum thickness is about ten times smaller than we are assuming. This occurs at $v \approx 60 \text{ km s}^{-1}$, corresponding to the peak in the cooling curve at 10^5 K (see § 2.5), since the thickness is set by the cooling length at higher speeds. In principle, the shell thickness can be measured observationally if the source is sufficiently well resolved (Kobulnicky et al. 2017), although this is complicated by projection effects.

Dust opacity The dust opacity will depend on the total dust-gas ratio and on the composition and size distribution of the grains. Our adopted value of $600 \text{ cm}^2 \text{ g}^{-1}$, or $1.3 \times 10^{-21} \text{ cm}^2 \text{ H}^{-1}$, is appropriate for average Galactic interstellar grains in the EUV and FUV (e.g., Weingartner & Draine 2001b), but there is ample evidence for substantial spatial variations in grain extinction properties (Fitzpatrick & Massa 2007), both on Galactic scales (Schlafly et al. 2016) and within a single star forming region (Beitia-Antero & Gómez de Castro 2017). The properties of grains within photoionized regions are very poorly constrained observationally because the optical depth is generally much lower than in overlying neutral material. In the Orion Nebula, there is some evidence (Salgado et al. 2016) that the FUV dust opacity in the ionized gas may be as low as $90 \text{ cm}^2 \text{ g}^{-1}$, although the uncertainties in this estimate are large and different results are obtained in other regions, such as W3(A) (Salgado et al. 2012).

Shell gas temperature For bows around O stars, the shell temperature should be close to the photoionization equilibrium value of $\approx 10^4 \text{ K}$, since the post-shock cooling length is short in ambient densities above 0.1 cm^{-3} (§ 2.5) and the shell does not trap the ionization front for ambient densities below 10^4 cm^{-3} (§ 2.4). For B stars, on the other hand, these two density limits move closer together (cf. the smaller gap between the blue and red lines in Figs. 2a and 4, as compared with 2b and c), making it more likely that a bow will lie in a different temperature regime. The only source for which we have evidence that this occurs is LP Ori, as discussed in the next section.

5.2.3 Special treatment of particular sources

For two of the additional bows listed in Table 4, we are forced to deviate from the default values for the shell parameters. For LP Ori, the bow shell appears to be formed from neutral gas (O'Dell 2001) and its relatively high τ value is more than sufficient to trap the weak ionizing photon output of a B3 star. We therefore move its point in Figure 13 downward to reflect a temperature of 1000 K (or, equivalently, a magnetically supported shell with $v_A \approx 3 \text{ km s}^{-1}$). For the case of the Orion Trapezium star θ^1 Ori D, we find that using the default parameters results in a placement well inside the forbidden zone of Figure 13 (indicated by fainter symbol). For this object there is no reason to suspect anything but the usual photoionized temperature of 10^4 K, but its placement could be resolved either by decreasing the shell thickness, or decreasing the UV dust opacity, or both. Given the moderate limb brightening seen in the highest resolution images of the Ney–Allen nebula (Robberto et al. 2005; Smith et al. 2005), the shell thickness is unlikely to be less than half our default value. But, if this were combined with a factor 5 decrease in κ , as suggested by Salgado et al. (2016), then this would be sufficient to move the source up to the RBW line, or slightly above.

5.3 Candidate radiation-supported bows

Four sources are sufficiently close to the diagonal line $\eta_{\text{sh}} = 1.25\tau$ in Figure 13 that they should be treated as potential candidates for radiation-supported bows. These are K18 sources 380 (HD 53367, V750 Mon) and 407 (HD 93249 in Carina) plus θ^1 Ori D and LP Ori.

5.4 Stellar wind mass-loss rates

Mass loss rates - starting from Kobulnicky et al. (2010)

Source 342 is anomalous in both methods.

Evidence for small grains around Arches cluster near Galactic center (?)

Different scenarios for producing velocities: dynamic ejection from young clusters (Hoogerwerf et al. 2001; Oh & Kroupa 2016) produce high velocities, dissolution of binary systems following core-collapse SN (Renzo et al. 2018) tend to produce lower velocities for the unbound MS companion (walkaways, slower than 30 km/s). Also, champagne flows have low velocities.

How different regions of the $\Pi-\Lambda$ plane are populated. Bottom-right quadrant hard to get to (except for standing wave oscillations), but may be due to finite shell thickness, which (for low Mach number) will be more apparent in the wings, which might decrease Λ more than Π . Fact that thin-shell solutions should trace the contact discontinuity, but in some cases it may be only the inner or the outer shell that is visible.

Justification for standing waves: Fig. 3 of Meyer et al. (2016) shows a time sequence of thin-shell instability, which looks a bit like a standing wave. But much larger amplitude than we are considering.

Deviations from axisymmetry as an alternative to oscillations.

5.5 The case of inside-out bows

So far, we have considered the case where the inner source dominates the radiation, while dust is present only in the outer stream, which applies to hot stars interacting with the ISM. However, in the case of cool stars, the inner wind will also be dusty. Examples are the red supergiant (RSG) phase of high-mass evolution, or the asymptotic giant branch (AGB) stage of low/intermediate-mass evolution. In

both these cases, it is still the inner source that provides the radiation field. However, not all winds are radiatively driven and in those cases it is conceivable that it is the outer source that dominates the radiation field. An example is the case of photoevaporating protoplanetary disks (proplyds) in the Orion Nebula and other H II regions (O'Dell & Wen 1994). In the proplyds, the inner wind is a thermally driven photoevaporation flow (Henney & Arthur 1998; Henney & O'Dell 1999), while the outer stream is the stellar wind from an O star (García-Arredondo et al. 2001).

6 SUMMARY AND CONCLUSIONS

REFERENCES

- Abel N. P., Hoof P. A. M. v., Shaw G., Ferland G. J., Elwert T., 2008, ApJ, 686, 1125
 Arthur S. J., Hoare M. G., 2006, ApJS, 165, 283
 Arthur S. J., Henney W. J., Mellema G., de Colle F., Vázquez-Semadeni E., 2011, MNRAS, 414, 1747
 Baines M. J., Williams I. P., Asebiomo A. S., 1965, MNRAS, 130, 63
 Baldwin J. A., Ferland G. J., Martin P. G., Corbin M. R., Cota S. A., Peterson B. M., Slettebak A., 1991, ApJ, 374, 580
 Balog Z., et al., 2014, Experimental Astronomy, 37, 129
 Beitia-Antero L., Gómez de Castro A. I., 2017, MNRAS, 469, 2531
 Bertoldi F., Draine B. T., 1996, ApJ, 458, 222
 Bohren C. F., Huffman D., 1983, Absorption and scattering of light by small particles. Wiley-VCH
 Brand J., Blitz L., 1993, A&A, 275, 67
 Brott I., et al., 2011, A&A, 530, A115
 Brown W. R., 2015, ARA&A, 53, 15
 Callingham J. R., Tuthill P. G., Pope B. J. S., Williams P. M., Crowther P. A., Edwards M., Norris B., Kedziora-Chudczer L., 2019, Nature Astronomy, 3, 82
 Canto J., Raga A. C., Wilkin F. P., 1996, ApJ, 469, 729
 Chandrasekhar I. S., 1941, ApJ, 93, 285
 Desert F.-X., Boulanger F., Puget J. L., 1990, A&A, 237, 215
 Draine B. T., 1981, ApJ, 245, 880
 Draine B. T., Li A., 2001, ApJ, 551, 807
 Draine B. T., Li A., 2007, ApJ, 657, 810
 Draine B. T., Salpeter E. E., 1979, ApJ, 231, 77
 Duley W. W., 1973, Ap&SS, 23, 43
 Engelbracht C. W., et al., 2007, PASP, 119, 994
 Fairlamb J. R., Oudmaijer R. D., Mendigutía I., Ille J. D., van den Ancker M. E., 2015, MNRAS, 453, 976
 Ferland G. J., et al., 2013, Rev. Mex. Astron. Astrofis., 49, 137
 Ferland G. J., et al., 2017, Rev. Mex. Astron. Astrofis., 53, 385
 Fitzpatrick E. L., Massa D., 2007, ApJ, 663, 320
 Gaia Collaboration et al., 2016, A&A, 595, A1
 Gaia Collaboration et al., 2018, A&A, 616, A1
 García-Arredondo F., Henney W. J., Arthur S. J., 2001, ApJ, 561, 830
 Giard M., Bernard J. P., Lacombe F., Normand P., Rouan D., 1994, A&A, 291, 239
 Gull T. R., Sofia S., 1979, ApJ, 230, 782
 Gvaramadze V. V., Alexashov D. B., Katushkina O. A., Kniazev A. Y., 2018, MNRAS, 474, 4421
 Habing H. J., 1968, Bull. Astron. Inst. Netherlands, 19, 421
 Hawley S. A., 1978, ApJ, 224, 417
 Henney W. J., Arthur S. J., 1998, AJ, 116, 322
 Henney W. J., O'Dell C. R., 1999, AJ, 118, 2350
 Hindmarsh A. C., 1983, IMACS Transactions on Scientific Computation, 1, 55
 Hoogerwerf R., de Bruijne J. H. J., de Zeeuw P. T., 2001, A&A, 365, 49
 Jones E., Oliphant T., Peterson P., et al., 2001–2019, SciPy: Open source scientific tools for Python, <http://www.scipy.org/>
 Katushkina O. A., Alexashov D. B., Izmodenov V. V., Gvaramadze V. V., 2017, MNRAS, 465, 1573

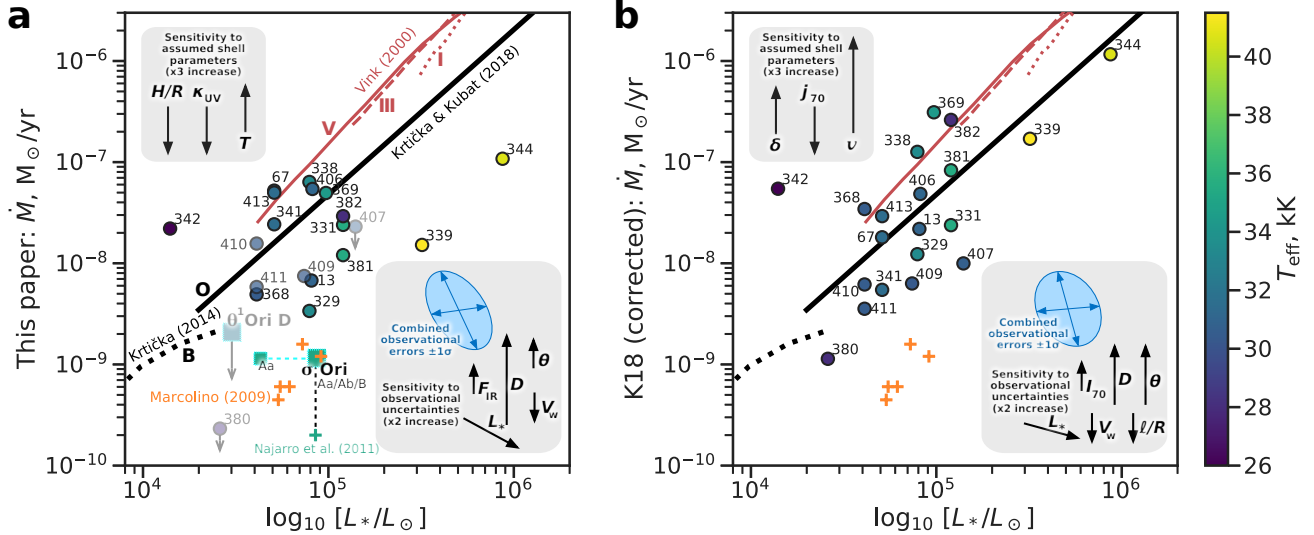


Figure 14. Wind mass-loss rates as a function of stellar luminosity, derived from (a) our trapped energy/momentum method and (b) the grain emissivity method of Kobulnicky et al. (2018), with corrections as described in our Appendix E. Circle symbols show the sources from K18, colored according to the stellar effective temperature (see key at far right). In panel a, squares show two of our additional sources (Tab. 4). Upper limits to the mass loss are given for sources that lie close to the radiation-supported line in Fig. 13, represented by faint symbols and downward-pointing arrows. Sources that lie less than a factor of three above the line have enhanced downward uncertainties and are also shown by slightly fainter symbols. For σ Ori, the large symbol corresponds to the sum of the luminosities of the triple OB system Aa, Ab, and B (Simón-Díaz et al. 2015), while the small symbol corresponds to the luminosity of only the most massive component Aa. Lines show the predictions of stellar wind models: red lines are the commonly used recipes from Vink et al. (2000) for dwarfs (solid), giants (dashed), and supergiants (dotted), while black lines show eq. (11) of Krtička & Kubát (2017) for O stars (solid) and models of Krtička (2014) for B stars. Orange plus symbols show mass-loss measurements from NUV lines for weak-wind O dwarfs (Marcolino et al. 2009), while the green plus symbol shows the measurement from infrared H recombination lines for σ Ori (Najarro et al. 2011). Boxes show the sensitivity of the results to observational uncertainties (lower right) and assumed shell parameters (upper left).

- Kobulnicky H. A., Gilbert I. J., Kiminki D. C., 2010, ApJ, 710, 549
Kobulnicky H. A., et al., 2016, ApJS, 227, 18
Kobulnicky H. A., Schurhammer D. P., Baldwin D. J., Chick W. T., Dixon D. M., Lee D., Povich M. S., 2017, AJ, 154, 201
Kobulnicky H. A., Chick W. T., Povich M. S., 2018, ApJ, 856, 74
Krtička J., 2014, A&A, 564, A70
Krtička J., Kubát J., 2017, A&A, 606, A31
Lamers H. J. G. L. M., Cassinelli J. P., 1999, Introduction to Stellar Winds. Cambridge, UK: Cambridge University Press
Lamers H. J. G. L. M., Snow T. P., Lindholm D. M., 1995, ApJ, 455, 269
Landau L., Lifshitz E., 1976, Mechanics, 3rd edn. Course of Theoretical Physics Vol. 1, Butterworth-Heinemann
Lanz T., Hubeny I., 2003, ApJS, 146, 417
Lanz T., Hubeny I., 2007, ApJS, 169, 83
Lebouteiller V., Bernard-Salas J., Whelan D. G., Brandl B., Galliano F., Charmandaris V., Madden S., Kunth D., 2011, ApJ, 728, 45
Lee E. J., Murray N., Rahman M., 2012, ApJ, 752, 146
Luri X., et al., 2018, A&A, 616, A9
Mac Low M.-M., van Buren D., Wood D. O. S., Churchwell E., 1991, ApJ, 369, 395
Marcolino W. L. F., Bouret J.-C., Martins F., Hillier D. J., Lanz T., Escolano C., 2009, A&A, 498, 837
Martins F., Schaerer D., Hillier D. J., 2005, A&A, 436, 1049
Mathis J. S., Mezger P. G., Panagia N., 1983, A&A, 128, 212
Matzner C. D., 2002, ApJ, 566, 302
Meyer D. M.-A., Mackey J., Langer N., Gvaramadze V. V., Mignone A., Izzard R. G., Kaper L., 2014, MNRAS, 444, 2754
Meyer D. M.-A., van Marle A.-J., Kuiper R., Kley W., 2016, MNRAS, 459, 1146
Meyer D. M.-A., Mignone A., Kuiper R., Raga A. C., Kley W., 2017, MNRAS, 464, 3229
Najarro F., Hanson M. M., Puls J., 2011, A&A, 535, A32
Nieva M.-F., 2013, A&A, 550, A26
O'Dell C. R., 2001, AJ, 122, 2662
O'Dell C. R., Wen Z., 1994, ApJ, 436, 194
Ochsendorf B. B., Tielens A. G. G. M., 2015, A&A, 576, A2
Ochsendorf B. B., Cox N. L. J., Krijt S., Salgado F., Berné O., Bernard J. P., Kaper L., Tielens A. G. G. M., 2014a, A&A, 563, A65
Ochsendorf B. B., Verdolini S., Cox N. L. J., Berné O., Kaper L., Tielens A. G. G. M., 2014b, A&A, 566, A75
Oh S., Kroupa P., 2016, A&A, 590, A107
Osokinova L. M., Todt H., Ignace R., Brown J. C., Cassinelli J. P., Hamann W.-R., 2011, MNRAS, 416, 1456
Osterbrock D. E., Ferland G. J., 2006, Astrophysics of gaseous nebulae and active galactic nuclei, second edn. Sausalito, CA: University Science Books
Pogodin M. A., Malanushenko V. P., Kozlova O. V., Tarasova T. N., Franco G. A. P., 2006, A&A, 452, 551
Prinja R. K., 1989, MNRAS, 241, 721
Puls J., Vink J. S., Najarro F., 2008, A&ARv, 16, 209
Quirez C., Rood R. T., Balser D. S., Bania T. M., 2006a, ApJS, 165, 338
Quirez C., Rood R. T., Bania T. M., Balser D. S., Maciel W. J., 2006b, ApJ, 653, 1226
Renzo M., et al., 2018, arXiv e-prints
Robberto M., et al., 2005, AJ, 129, 1534
Rodríguez-Ramírez J. C., Raga A. C., 2016, MNRAS, 460, 1876
Salgado F., et al., 2012, ApJ, 749, L21
Salgado F., Berné O., Adams J. D., Herter T. L., Keller L. D., Tielens A. G. G. M., 2016, ApJ, 830, 118
Schlafly E. F., et al., 2016, ApJ, 821, 78
Simón-Díaz S., et al., 2015, ApJ, 799, 169
Smith N., Bally J., Shuping R. Y., Morris M., Kassis M., 2005, AJ, 130, 1763

- Spitzer L., 1978, Physical processes in the interstellar medium. New York: Wiley-Interscience
- Stark A. A., 1984, ApJ, 281, 624
- Sternberg A., Hoffmann T. L., Pauldrach A. W. A., 2003, ApJ, 599, 1333
- Tarango-Yong J. A., Henney W. J., 2018, MNRAS, 477, 2431
- Tenorio-Tagle G., 1979, A&A, 71, 59
- Tielens A. G. G. M., Hollenbach D., 1985, ApJ, 291, 722
- Tjin A Djie H. R. E., van den Ancker M. E., Blondel P. F. C., Shevchenko V. S., Ezhkova O. V., de Winter D., Grankin K. N., 2001, MNRAS, 325, 1441
- Tuthill P. G., Monnier J. D., Danchi W. C., 1999, Nature, 398, 487
- Vink J. S., de Koter A., Lamers H. J. G. L. M., 1999, A&A, 350, 181
- Vink J. S., de Koter A., Lamers H. J. G. L. M., 2000, A&A, 362, 295
- Weidenschilling S. J., 1977, MNRAS, 180, 57
- Weingartner J. C., Draine B. T., 2001a, ApJS, 134, 263
- Weingartner J. C., Draine B. T., 2001b, ApJ, 548, 296
- Weingartner J. C., Draine B. T., Barr D. K., 2006, ApJ, 645, 1188
- Wilkin F. P., 1996, ApJ, 459, L31
- Xie Y., Ho L. C., Li A., Shangguan J., 2018, ApJ, 867, 91
- de Jager C., Nieuwenhuijzen H., van der Hucht K. A., 1988, A&AS, 72, 259
- van Buren D., McCray R., 1988, ApJ, 329, L93
- van Hoof P. A. M., Weingartner J. C., Martin P. G., Volk K., Ferland G. J., 2004, MNRAS, 350, 1330
- van Leeuwen F., 2007, A&A, 474, 653
- van Marle A. J., Meliani Z., Keppens R., Decin L., 2011, ApJ, 734, L26

APPENDIX A: GRAIN CHARGING AND GAS–GRAIN COUPLING AROUND OB STARS

We calculate models of the physical properties of dust grains using the plasma physics code Cloudy (Ferland et al. 2013, 2017), which self-consistently solves the multi-frequency radiative transfer together with thermal, ionization, and excitation balance of all plasma constituents. Cloudy incorporates grain charging as described in Baldwin et al. (1991) and van Hoof et al. (2004) with photoelectric emission theory from Weingartner & Draine (2001a); Weingartner et al. (2006). We use the default “ISM” dust mixture included in Cloudy, which comprises ten size bins each for spherical silicate and graphite grains in the range 0.005 to 0.25 μm , and which is designed to reproduce the average Galactic extinction curve (Weingartner & Draine 2001b; Abel et al. 2008). The optical properties of each grain species are calculated using Mie theory (Bohren & Huffman 1983), assuming solid spheres. The resultant wavelength-dependent extinction properties of the mixture are summarised in Figure A1.

To ascertain the expected variation in grain properties in the circumstellar environs of luminous stars, we calculate a series of spherically symmetric, steady-state, constant density Cloudy simulations, illuminated by the stars listed in Table 1, with stellar spectra taken from the OSTAR2002 and BSTAR2006 grids, calculated with the TLUSTY model atmosphere code (Lanz & Hubeny 2003, 2007). Simulations are run for hydrogen densities of 1, 10, 100, 10^3 and 10^4 cm^{-3} and assuming standard H II region gas phase abundances. The calculation is stopped when the ionization front is reached and the inner radius is chosen to be roughly 1% of this.

Figure A2 shows resultant radial profiles of dust properties for representative simulations: grain temperature, grain abundance, grain potential, and grain drift velocity. Line types correspond to the different size bins of graphite and silicate grains, as indicated in the key from smallest to largest. The left hand panels show results for a high-density ($n = 10^4 \text{ cm}^{-3}$), compact ($R \approx 0.1 \text{ pc}$) region around an early O star, where the grain temperature is very high, especially for the smaller silicate grains, and sublimation significantly reduces the grain abundance in the inner regions. The remaining columns

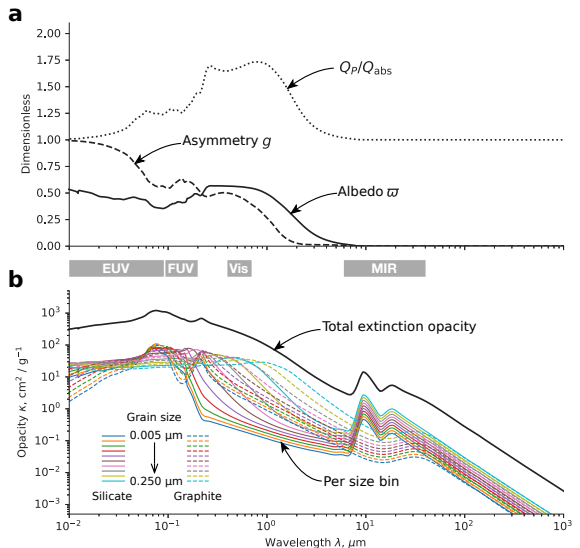


Figure A1. Extinction properties of Cloudy’s standard “ISM” dust mixture. (a) Wavelength dependence of mean values over the entire mixture of three dimensionless quantities related to scattering: albedo, ω (solid line); scattering asymmetry, $g = \langle \cos \theta \rangle$ (dashed line); ratio of radiation pressure efficiency to absorption efficiency, Q_P/Q_{abs} (dotted line). (b) Wavelength dependence of mass opacity (cross section per unit mass of gas) for the whole mixture (heavy black line) and broken down by size bin and grain composition (colored lines, see key).

show low-density ($n = 1 \text{ cm}^{-3}$), extended ($R \sim 10 \text{ pc}$) regions around main-sequence and supergiant B-type stars, in which the grain temperatures are much lower, ranging from 20 K to 50 K in the outer parts up to 100 K to 200 K in the inner parts.

Unlike the strong differences in thermal properties, the radial dependence of grain electrostatic potential (third row in Fig. A2) is qualitatively similar for all the simulations. The grains are predominantly positively charged, with high potentials (> 10 times the thermal energy of gas particles) close to the star due to the strong EUV and FUV photo-ejection. The potential falls to much lower values in the outer ionized region, as the EUV flux falls off, and then climbs again at the ionization front due to the fall in electron density, while the FUV photo-ejection persists well into the neutral region. There are small differences between the simulations due to the increasing relative importance of the EUV radiation for hotter stars, which leads to a deeper dip in the potential just inside the ionization front for the $40 M_\odot$ case, even reaching negative values for some grain species.

Equilibrium drift velocity for each grain species is calculated in the Cloudy simulations using the same theory (Draine & Salpeter 1979) as outlined in § 3.1. The way that this is implemented by default in Cloudy means that if the only solution at the inner radius is a superthermal one, then the superthermal solution branch (upper right corner of Fig. 7) is followed as far as possible through the outer spatial zones. We have modified the code so as to instead always prefer the slower subthermal branch whenever multiple solutions are available. This makes the most sense in our context, where the grains are moving towards the star and so the radiative force is gradually increasing from an initial low value. Example results are shown in the bottom row of Figure A2 and again they are qualitatively similar for all the simulations. Close to the star, the radiation force is higher

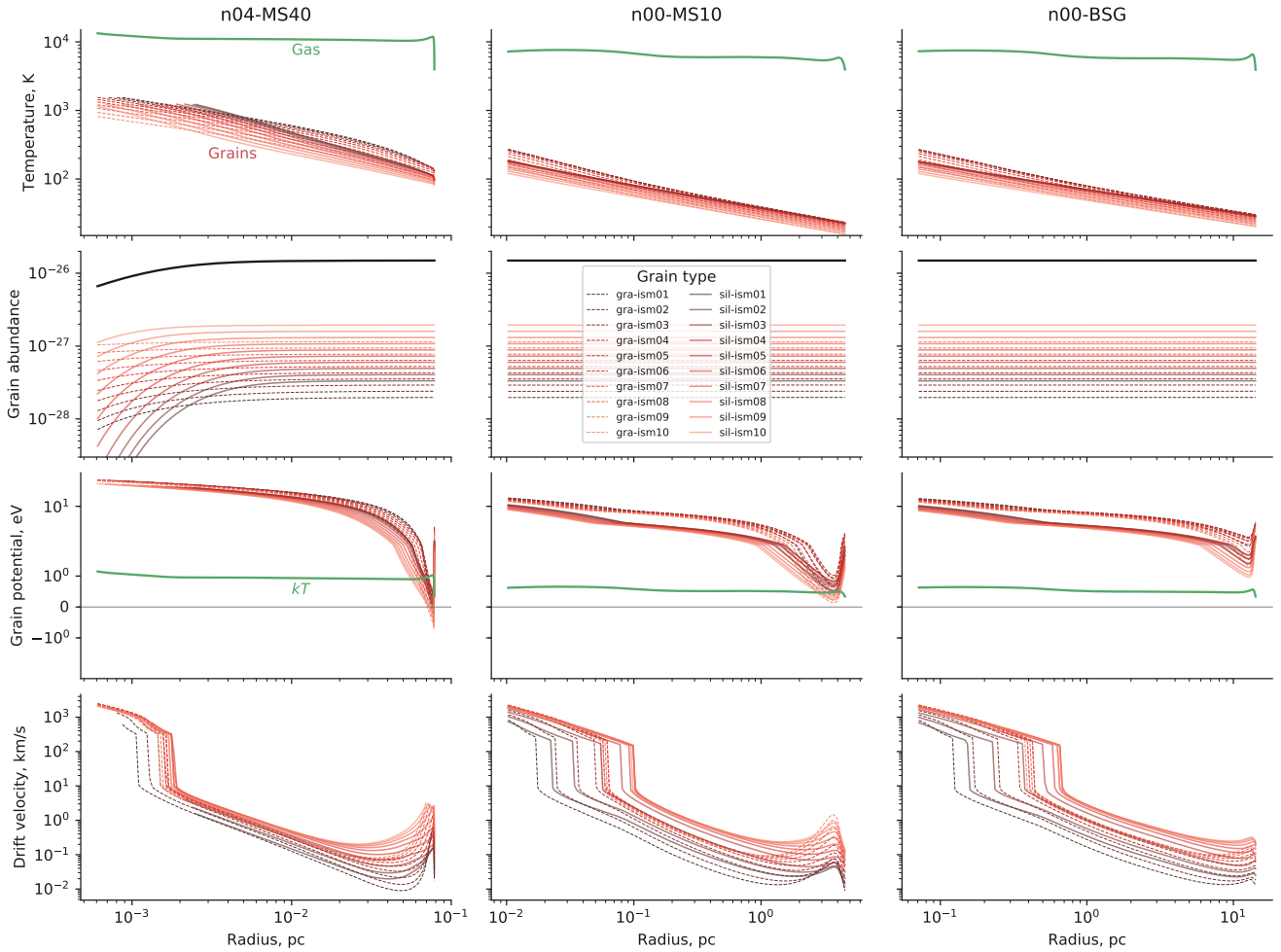


Figure A2. Dust properties as a function of radius from star for three selected Cloudy simulations. (a) $40 M_{\odot}$ main-sequence star in medium of density 10^4 cm^{-3} . (b) $10 M_{\odot}$ main-sequence star in medium of density 1 cm^{-3} . (c) Blue supergiant star in medium of density 1 cm^{-3}

than the upper limit on the Coulomb drag force (eq. [38]), so that the equilibrium drift velocity is exceedingly high.²⁰ As the radial distance from the star increases, the radiation field is increasingly diluted but the grain potential falls only slowly, so eventually one reaches a point where an equilibrium between Coulomb drag and radiation force can be established, which corresponds to a discontinuity in the drift velocity. This is the *rip point* discussed in § 3.2. The drift velocity carries on falling towards the outside of the H II region, but then increases again just inside the ionization front due to the drop in grain potential there.

Both the charge balance and the force balance are essentially due to competition between the photons and the charged particles that interact with the grain. It is therefore reasonable to surmise that the gas–grain decoupling that occurs at the rip point might be determined principally by the ratio of photons to gas particles.

²⁰ Note that such high drift velocities are much higher than any realistic true relative velocity between grains and gas, since they are based on the assumption that the radiation force remains constant while the grain is accelerated, which is not the case near the rip point. Instead, they are simply an indication that the gas and grains have completely decoupled.

We test this hypothesis in Figure A3, where we characterize the photon-gas ratio by a dimensionless radiation parameter, Ξ , equal to the radiation pressure divided by the gas pressure. Results are shown for four different grain types and for all combinations of stellar parameters and ambient densities for which we have run simulations. It can be seen that the rip point does indeed always occur at a similar value of $\Xi \sim 1000$ for all simulations, albeit with some variation according to the spectral type of the star and the grain composition, as given in Table 3. The gas density and grain size have very little influence on this critical value Ξ_{\dagger} , with the only exception being the very smallest grains ($a < 0.006 \mu\text{m}$, not illustrated), which show $\Xi_{\dagger} \approx 10^4$, but such grains are only minor contributors to the UV opacity (< 10% in EUV and < 1% in FUV, see Fig. A1).

Finally, Figure A4 shows the slow dependence of grain potential on radiation parameter for all the simulations on a linear versus logarithmic scale. The logarithmic fit of equation (41), most appropriate for carbon grains around cooler stars, is shown by the solid line. The dashed lines show the modifications for silicate grains and for hotter stars (see § 3.2). Further details of the Cloudy dust models are discussed in Appendix B.

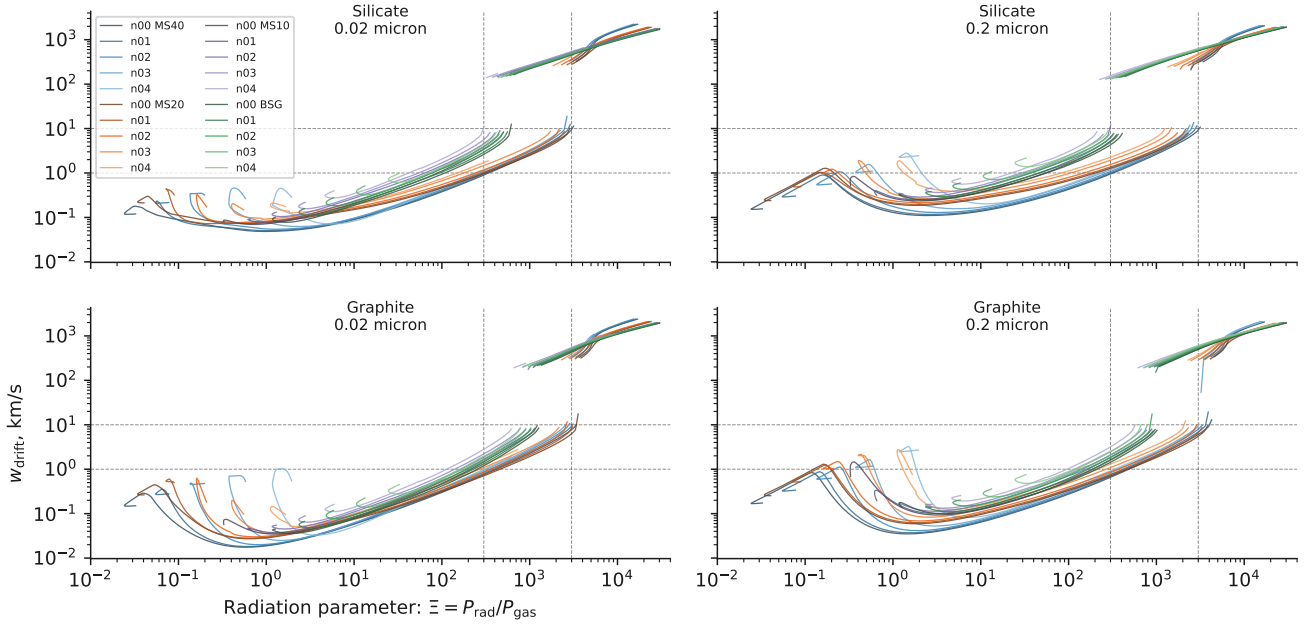


Figure A3. Drift velocity w_{drift} versus radiation parameter Ξ . Each line represents a simulation with ambient density and stellar type as indicated in the key. Results are shown for graphite and silicate grains of two different sizes. The rip point, which corresponds to gas–grain decoupling, is the discontinuity in the curves at $w_{\text{drift}} \approx 10 \text{ km s}^{-1}$, indicated by the upper horizontal dashed line. The vertical dashed lines show the narrow range of radiation parameter, $\Xi = 1000 \pm 0.5 \text{ dex}$, that encompasses the rip point for all simulations.

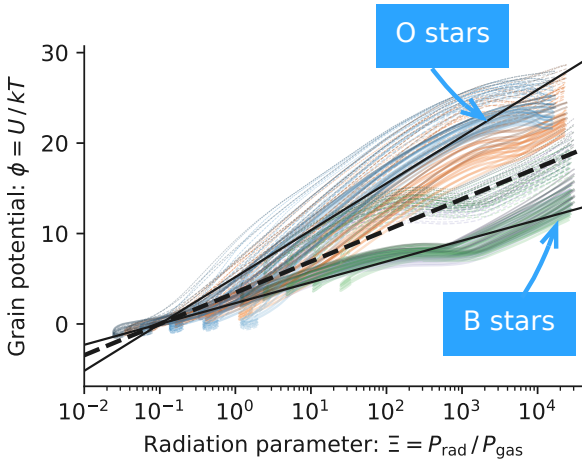


Figure A4. Grain potential in thermal units (linear scale) versus radiation parameter (logarithmic scale). All densities and stellar types are shown, with line colors as in Fig. A3. Solid lines show silicate grains and dashed lines show graphite grains. Line width increases with grain size (to reduce clutter, only every second size bin is shown). The solid and dashed lines show the logarithmic fits discussed in the text.

APPENDIX B: GRAIN TEMPERATURE AND MID-INFRARED EMISSIVITY

Figure B1 shows equilibrium grain temperatures for the Cloudy models discussed in Appendix A as a function of the nominal energy density of the radiation field, $U = u/u_{\text{MMP83}}$, where $u = L/4\pi R^2 c$

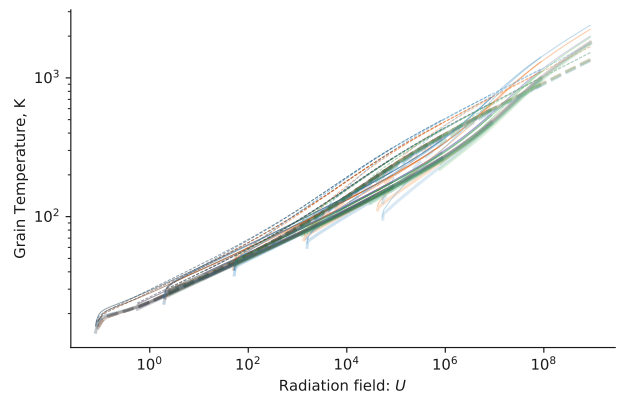


Figure B1. Grain temperature versus radiation field mean intensity, U , in units of the interstellar radiation field in the solar neighborhood. Line types and colors are as in Fig. A4 and correspond to a variety of stellar spectral shapes, gas densities, and grain species.

and u_{MMP83} is the energy density of the interstellar radiation field for $\lambda < 8 \mu\text{m}$ in the solar neighborhood (Mathis et al. 1983):

$$u_{\text{MMP83}} c = 0.0217 \text{ erg s}^{-1} \text{ cm}^{-2}. \quad (\text{B1})$$

The tight relationship seen in figure B1 between T and U is evidence for the dominance of stellar radiative heating (see § B1 below), while the variation about the mean relation is mainly due to differences in grain size and composition, with smaller grains and graphite grains being relatively hotter. The downward hooks seen on the left end of each simulation’s individual curve are due to the fact that our

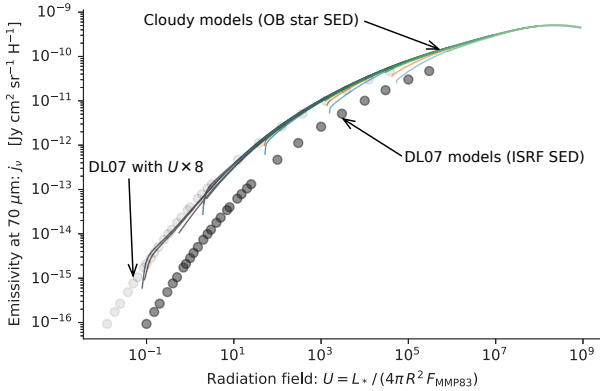


Figure B2. Grain emissivity at 70 μm for all Cloudy models (lines colored as in Fig. A3), compared with grain models from Draine & Li (2007) (dark gray symbols), which assume illumination by a scaled interstellar radiation field, which has a SED with a very different shape from that of an OB star, see Fig. B3.

calculation of U does not account for internal absorption, which starts to become important near the ionization front.

The grain emissivity at 70 μm (Herschel PACS blue band) for the Cloudy simulations (colored lines) is shown in Figure B2, where it is compared with the same quantity from the grain models (dark gray symbols) of Draine & Li (2007). A clear difference is seen between the two sets of models, but this is due almost entirely to a difference in the assumed spectrum of the illuminating radiation, as illustrated in Figure B3. Draine & Li (2007) use a SED that is typical of the interstellar radiation field in the Galaxy, which is dominated by an old stellar population, which peaks in the near infrared, with only a small FUV contribution from younger stars (about 8% of the total energy density). This is very different from the OB star SEDs, which are dominated by the FUV and EUV bands. Since the grain absorption opacity is much higher at UV wavelengths than in the visible/IR (see Fig. A1), the effective grain heating efficiency of the OB star SED is correspondingly higher. The light gray symbols show the effect on the Draine & Li (2007) models of multiplying the radiation field by a factor of 8 in order to offset this difference in efficiency, which can be seen to bring them into close agreement with the Cloudy models. A further difference is that the Draine & Li (2007) model includes small PAH particles, which we do not include in our Cloudy models, since they are believed to be largely absent in photoionized regions (Giard et al. 1994; Lebouteiller et al. 2011). However, this only effects the emissivity at shorter mid-infrared wavelengths $< 20 \mu\text{m}$.

In terms of the characteristic parameters introduced in § 2.2 the dimensionless radiation field becomes

$$U = 14.7 L_4 R_{\text{pc}}^{-2}, \quad (\text{B2})$$

or, alternatively, it can be expressed in terms of the ambient stream as

$$U = 3.01 n v_{10}^2 / x^2, \quad (\text{B3})$$

where $x = R_0 / R_*$ is given by equation (12). It can also be related to the radiation parameter Ξ , defined in equation (40), as

$$U = 3.82 n T_4 \Xi. \quad (\text{B4})$$

A common alternative approach to scaling the radiation field (see

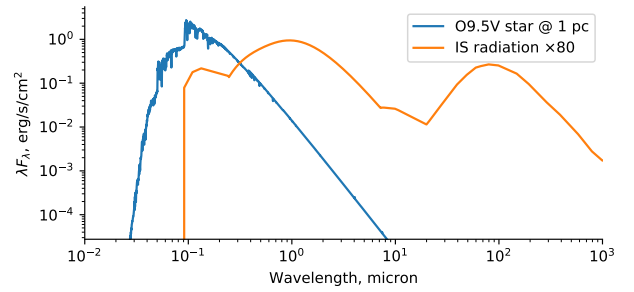


Figure B3. Comparison between the spectral energy distribution (SED) of a typical OB star (blue line) and the interstellar radiation field in the solar neighborhood (orange line). The OB star is the $20 M_\odot$ model from Table 1 and is plotted for a distance from the star of 1 pc. The interstellar SED is from Mathis et al. (1983) and is multiplied by 80 so that the total FUV-to-NIR flux is equal for the two SEDs.

Tielens & Hollenbach 1985 and citations thereof) is to normalize in the FUV band ($0.0912 \mu\text{m}$ to $0.24 \mu\text{m}$), where the local interstellar value is known as the Habing flux (Habing 1968):

$$F_{\text{Habing}} = 0.0016 \text{ erg s}^{-1} \text{ cm}^{-2}. \quad (\text{B5})$$

The resultant dimensionless flux is often denoted by G_0 , and the relationship between G_0 and U depends on the fraction f_{fuv} of the stellar luminosity that is emitted in the FUV band:

$$G_0 = f_{\text{fuv}} \frac{u_{\text{MMP83}} c}{F_{\text{Habing}}} U = (6 \text{ to } 10) U, \quad (\text{B6})$$

where we give the range corresponding to early O ($f_{\text{fuv}} \approx 0.4$) to early B ($f_{\text{fuv}} \approx 0.7$) stars.

B1 Unimportance of other heating mechanisms

The grain temperature in bows around OB stars is determined principally by the steady-state equilibrium between the absorption of stellar UV radiation (heating) and the thermal emission of infrared radiation (cooling). Other processes such as single-photon stochastic heating, Lyman α line radiation, and post-shock collisional heating can dominate in other contexts, but these are generally unimportant for circumstellar bows, as we now demonstrate.

B1.1 Stochastic single-photon heating

When the radiation field is sufficiently dilute, then a grain that absorbs a photon has sufficient time to radiate all that energy away before it absorbs another photon (Duley 1973). In this case, the emitted infrared spectrum for $\lambda < 50 \mu\text{m}$ becomes relatively insensitive of the energy density of the incident radiation (Draine & Li 2001). However, this is most important for the very smallest grains. From equation (47) of Draine & Li (2001), one finds that grains with sizes larger than $a = 0.005 \mu\text{m} = 5 \text{ nm}$ (the smallest size included in our Cloudy models) should be close to thermal equilibrium for $U > 30$, which is small compared with typical bow shock values ($U = 10^3$ to 10^6). As mentioned above, PAHs are not expected to be present in the interior of H II regions. Desert et al. 1990 found them to be strongly depleted for $U > 100$ around O stars. However, other types of ultra-small grains, down to sub-nm sizes (Xie et al. 2018) may be present in bows, and stochastic heating would be important for grains with $a = 1 \text{ nm}$ if $U < 10^5$. Note, however that

grains smaller than 0.6 nm would be destroyed by sublimation after absorbing a single He-ionizing photon.

B1.2 Lyman α heating

On the scale of an entire H II region, the dust heating is typically dominated by Lyman α hydrogen recombination line photons, which are trapped by resonant scattering (e.g., Spitzer 1978 § 9.1b). However, this is no longer true on the much smaller scale of typical bow shocks. An upper limit on the Lyman α energy density can be found by assuming all line photons are ultimately destroyed by dust absorption rather than escaping in the line wings (e.g., Henney & Arthur 1998), which yields

$$U_{\text{Ly}\alpha} \approx 0.1n/\kappa_{600}. \quad (\text{B7})$$

This can be combined with equation (B3) to give the ratio of Lyman α to direct stellar radiation as

$$\frac{U_{\text{Ly}\alpha}}{U} \approx 0.03 \frac{x^2}{v_{10}^2 \kappa_{600}}. \quad (\text{B8})$$

Taking the most favorable parameters imaginable of a slow stream ($v_{10} = 2$), very strong wind ($x \approx 1$), and reduced dust opacity ($\kappa_{600} = 0.1$) gives a Lyman α contribution of only 10% of the stellar radiative energy density. In any other circumstances, the fraction would be even lower.

B1.3 Shock heating

The outer shock thermalizes the kinetic energy of the ambient stream, which may in principle contribute to the infrared emission of the bow. In order for this process to be competitive, the following three conditions must all hold:

1. The post-shock gas must radiate efficiently with a cooling length less than the bow size, see § 2.5. This is satisfied for all but the lowest densities (see Fig. 2).
2. A significant fraction of the shock energy must be radiated by dust. This requires that the post-shock temperature be greater than 10^6 K, which requires a stream velocity $v > 200$ km s $^{-1}$ (Draine 1981). This also coincides with the range of shock velocities where the smaller grains will start to be destroyed by sputtering in the post-shock gas.
3. The kinetic energy flux through the shock must be significant, compared with the fraction of the stellar radiation flux that is absorbed and reprocessed by the bow shell.

It turns out that the third condition is the most stringent, so we will consider it in detail. The kinetic energy flux through the outer shock for an ambient stream of density ρ and velocity v is

$$F_{\text{kin}} = \frac{1}{2} \rho v^3 = \frac{1}{2} P_{\text{sh}} v, \quad (\text{B9})$$

while the stellar radiative energy flux absorbed by the shell is

$$F_{\text{abs}} \approx \tau L / 4\pi R_0^2, \quad (\text{B10})$$

assuming an absorption optical depth $\tau \ll 1$. The shell pressure in the WBS case can be equated to the ram pressure of the internal stellar wind (see § 2.1), so that the ratio of the two energy fluxes is

$$\frac{F_{\text{kin}}}{F_{\text{abs}}} = \frac{1}{2} \frac{\eta_w}{\tau} \frac{v}{c}. \quad (\text{B11})$$

An upper limit to the stellar wind momentum efficiency η_w is the shell momentum efficiency η_{sh} that is derived observationally in § 5, where

it is found that $\eta_{\text{sh}}/\tau < 30$ for all sources considered. Therefore, for a stream velocity $v = 200$ km s $^{-1}$, we have $F_{\text{kin}}/F_{\text{abs}} < 0.01$ and the shock-excited dust emission is still negligible. Only in stars with $v > 1000$ km s $^{-1}$ would the shock emission start to be significant, and such hyper-velocity stars (Brown 2015) do not show detectable bow shocks.

So far, we have only considered the outer shock, but the inner shock that decelerates the stellar wind will have a velocity of 1000 km s $^{-1}$ to 3000 km s $^{-1}$ and therefore might have a significant kinetic energy flux by eq. (B11). However, the stellar wind from hot stars will be free of dust,²¹ so that it would be necessary for the stellar wind protons to cross the contact/tangential discontinuity and deposit their energy in the dusty plasma of the shocked ambient stream. This is not possible because the Larmor radius (see § 4) of a 3000 km s $^{-1}$ proton in a 1 μ G field is only 3×10^{10} cm, which is millions of times smaller than typical bow sizes. The magnetic field in the outer shell is unlikely to be smaller than $\approx n^{1/2} \mu$ G, given that Alfvén speeds of 2 km s $^{-1}$ are typical of photoionized regions (cf. eq. [54]) and if the density were much lower than 1 cm $^{-3}$, then the scale of the bow would be commensurately larger anyway. Three-dimensional MHD simulations of bow shocks (Katushkina et al. 2017; Gvaramadze et al. 2018) show that the magnetic field lines are always oriented parallel to the shell, so that high energy particles from the stellar wind would be efficiently reflected in a very thin layer and cannot contribute to grain heating. For the same reason, heat conduction by electrons across the contact discontinuity is also greatly suppressed (Meyer et al. 2017).

APPENDIX C: DUST WAVES IN THE DRAG-FREE LIMIT

A dust grain of geometrical cross-section σ_d situated a distance R from a point source of radiation with luminosity L will experience a repulsive, radially directed radiative force (e.g., Spitzer 1978)

$$f_{\text{rad}} = \frac{\sigma_d Q_p L}{4\pi R^2 c} e^{-\tau} \quad (\text{C1})$$

where Q_p is the frequency-averaged²² radiation pressure efficiency²³ of the grain, c is the speed of light, and τ is the frequency-averaged optical depth between the source and the grain. For simplicity, we will consider only the optically thin case, $\tau \rightarrow 0$.

If f_{rad} is the only force experienced by the grain, then it will move on a *ballistic* trajectory, determined by its initial speed at large distance, v_∞ , and its impact parameter, b . For $b = 0$, the grain radially approaches the source with initial radial velocity $-v_\infty$, which is decelerated to zero at the distance of closest approach, R_{**} , given by energy conservation:

$$R_{**} = \frac{\sigma_d Q_p L}{2\pi c m_d v_\infty^2}, \quad (\text{C2})$$

where m_d is the grain mass. The grain then turns round and recedes from the source along the same radius, reaching a velocity of $+v_\infty$ at large distance. Note that R_{**} as given by equation (C2) is the

²¹ With the exception of Wolf-Rayet colliding wind binary systems (Tuthill et al. 1999; Callingham et al. 2019).

²² Frequency averages of any quantity x should be understood as weighted by the attenuated source spectrum: $\langle x \rangle_\nu = (L e^{-\tau})^{-1} \int_0^\infty x(\nu) L_\nu e^{-\tau_\nu} d\nu$.

²³ For absorption efficiency Q_{abs} , scattering efficiency Q_{scat} , and asymmetry parameter (mean scattering cosine) g , we have $Q_p = Q_{\text{abs}} + (1 - g)Q_{\text{scat}}$ (e.g., § 4.5 of Bohren & Huffman 1983).

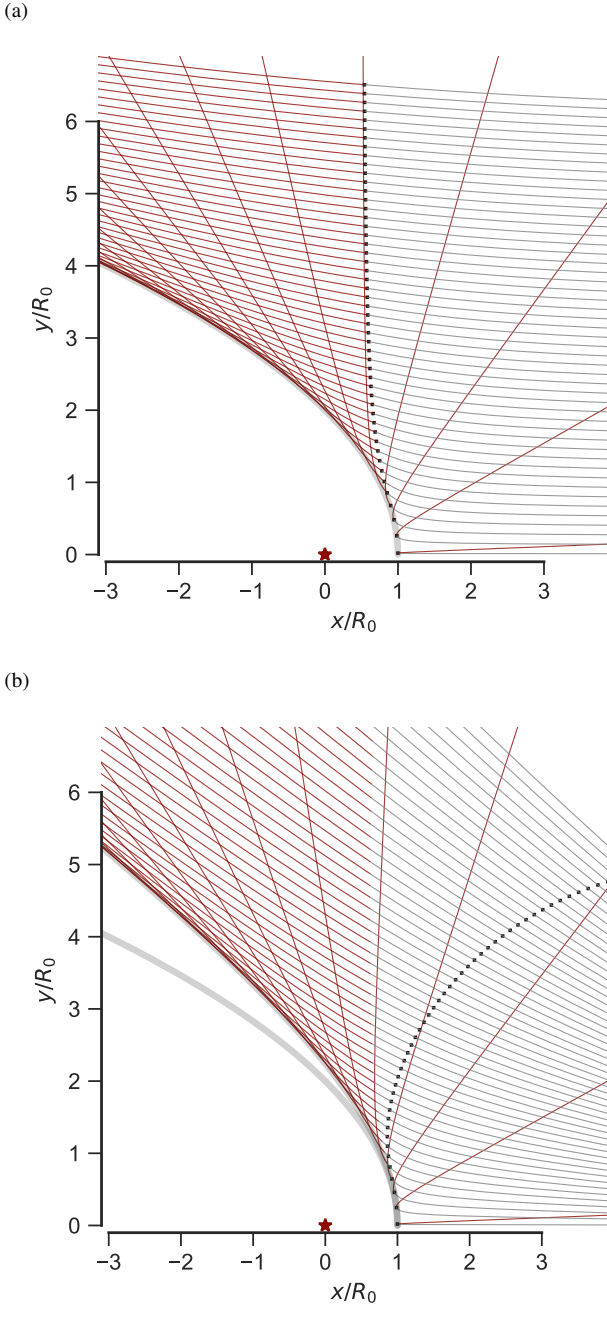


Figure C1. Dust grain trajectories under influence of a repulsive central r^{-2} radiative force. (a) A parallel stream of dust grains approach from the right at a uniform velocity and with a variety of impact parameters (initial y -coordinate). The central source is marked by a red star at the origin, and its radiative force deflects the trajectories into a hyperbolic shape, each of which reaches a minimum radius marked by a small black square. The incoming hyperbolic trajectories are traced in gray and the outgoing trajectories are traced in red. The locus of closest approach of the outgoing trajectories is parabolic in shape (traced by the thick, light gray line) and this constitutes the inner edge of the bow wave. (b) The same but for a divergent stream of dust grains that originates from a source on the x axis at a distance $D = 10R_{**}$ from the origin. In this case, the inner edge of the bow wave is hyperbolic and the parallel stream result is also shown for comparison.

equivalent of equation (6), except for a single grain considered in isolation, rather than a well-coupled dusty plasma.

For $b > 0$, the trajectory, $R_d(\theta; b)$, is found²⁴ to be hyperbolic, characterized by an eccentricity, $\varepsilon = (1 + 4b^2/R_{**}^2)^{1/2}$, and polar angle of closest approach, $\theta_m = \cos^{-1} \varepsilon^{-1}$. The trajectory is symmetrical about θ_m and can be written as

$$\frac{R_d(\theta; b)}{R_{**}} = \frac{\frac{1}{2}(\varepsilon^2 - 1)}{\varepsilon \cos(\theta - \theta_m) - 1}, \quad (\text{C3})$$

with a total deflection angle of $180^\circ - 2\theta_m$, which is equal to 90° when $b = 0.5R_{**}$.

C1 Parallel dust stream

If the incoming dust grains initially travel along parallel trajectories with varying b , but the same v_∞ , then deflection by the radiative force will form a bow-shaped dust wave around the radiation source, as shown in Figure C1. However, the inner edge of the dust wave, $R_{\text{in}}(\theta)$ is not given by the closest approach along individual trajectories, $R_d(\theta_m; b)$, but instead must be found by minimizing $R_d(\theta; b)$ over all b for each value of θ , which yields

$$\frac{R_{\text{in}}(\theta)}{R_{**}} = \frac{2}{1 + \cos \theta}. \quad (\text{C4})$$

This is the polar form of the equation for the confocal parabola, which we have already discussed in detail in § 4 and Appendix C of Tarango-Yong & Henney (2018). Its planitude and alatitude are $\Gamma = \Lambda = 2$ and these are unchanged under projection at any inclination.

C2 Divergent dust stream

If the dust grains are assumed to originate from a second point source, located at a distance D from the radiation source, then the incoming stream will be divergent instead of plane parallel. The individual streamlines are not affected by this change and are still described by equation (C3), except that the trajectory axes for $b > 0$ are no longer aligned with the global symmetry axis, so we must make the substitution $\theta \rightarrow \theta + \theta_1(b)$, where $\sin \theta_1 = b/D$ (see Fig. 3 of Paper I). We parametrize the degree of divergence as $\mu = R_{**}/D$ and, as before, $R_d(\theta + \theta_1(b, \mu); b)$ is minimized over all trajectories to find the shape of the bow wave's inner edge. This time, the result is a confocal hyperbola:

$$\frac{R_{\text{in}}(\theta; \mu)}{R_{**}} = \frac{1 + \varepsilon_\mu}{1 + \varepsilon_\mu \cos \theta}, \quad (\text{C5})$$

where the eccentricity is (to first order in μ) $\varepsilon_\mu = (1 - 2\mu)^{-1}$. An example is shown in Figure C1 for $\mu = 0.1$. Unsurprisingly, the resulting bow shape is more open than in the parallel stream case, increasingly so with increasing μ . The planitude and alatitude are both equal: $\Pi = \Lambda = 1 + \varepsilon_\mu$.

C3 Tight magnetic coupling

As discussed in § 4, for small grains ($a < 0.1 \mu\text{m}$) the Larmor magnetic gyration radius, r_B is typically small compared with other

²⁴ The problem is formally identical to that of Rutherford scattering, or (modulo a change of sign) planetary orbits. The method of solution (via introduction of a centrifugal potential term and reduction to a 1-dimensional problem) can be found in any classical mechanics text (e.g., Landau & Lifshitz 1976, § 14).

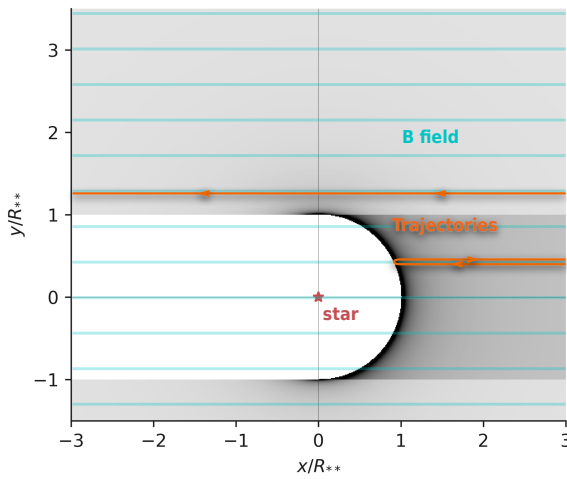


Figure C2. Dust wave formed by action of radiation forces on grains that are tightly coupled to a uniform parallel magnetic field. Two example trajectories, one with $b > R_{**}$ (upper) and one with $b < R_{**}$ (lower) are shown schematically in orange. The orientation of the magnetic field lines is shown in blue. The grayscale image shows the resultant dust density distribution.

length scales of interest, and so the grains are effectively tied to the magnetic field lines. In this approximation, we can calculate the grain dynamics in the drag-free limit using f_{rad} as the sole force as above, but this time allowing acceleration only along the field lines. Assuming a uniform magnetic field, the only extra parameter needed is θ_B , the angle between the field direction and the direction of the dust stream (assumed to be plane parallel). The radiation force will also produce an out-of-plane drift, given by

$$\mathbf{v}_{\text{drift}} = \frac{c}{ez_d} \frac{\mathbf{f}_{\text{rad}} \times \mathbf{B}}{B^2}, \quad (\text{C6})$$

but from equations (53, C1, C2) it follows that

$$\frac{v_{\text{drift}}(R_{**})}{v_\infty} = \frac{r_B}{2R_{**}}, \quad (\text{C7})$$

so it is valid to ignore this drift in the limit of small r_B .

We now calculate in detail the grain trajectories in this limit for two cases, with the magnetic field oriented parallel and perpendicular to the stream²⁵ direction, respectively. These are sufficient to give a flavor of the effects of a magnetic field on the dust wave structure. Further models at intermediate angles, and which also include the effects of gas drag, are presented in § 4.

C3.1 Parallel magnetic field

For $\theta_B = 0$, the $b = 0$ trajectory is identical to the non-magnetic case since the grain velocity and radiation force are both parallel to the field, which yields zero Lorentz force and zero $\mathbf{f} \times \mathbf{B}$ drift. Therefore, the axial turnaround radius, R_{**} , is still given by equation (C2), whatever the value of r_B . For $b > 0$, f_{rad} has a component perpendicular to \mathbf{B} , which will induce a helical gyromotion around the field lines, but the guiding center must move parallel to the axis

²⁵ In both cases, the stream trajectories are assumed parallel to one another, as in § C1.

if $r_B \ll R_{**}$. Thus, the guiding center motion can be found from conservation of potential plus kinetic energy in one dimension:

$$\frac{v^2}{v_\infty^2} + V_{\text{rad}} = 1, \quad (\text{C8})$$

where V_{rad} is a suitably normalized potential of the projected radiation force along the field lines (x axis, where $x = R \cos \theta = b \cot \theta$):

$$V_{\text{rad}} = R_{**} \int_x^\infty \frac{\cos \theta}{R^2} dx = \frac{R_{**} \sin \theta}{b} = \frac{R_{**}}{R}. \quad (\text{C9})$$

From equation (C8), the trajectory must turn around when $V_{\text{rad}} = 1$, and equation (C9) shows that this occurs at the same spherical radius, $R = R_{**}$, for all impact parameters, b , so that the inner boundary of the dust wave is hemispherical in shape:

$$\frac{R_{\text{in}}(\theta)}{R_{**}} = 1, \quad (\text{C10})$$

yielding planitude and alatitude of $\Pi = \Lambda = 1$. Note, however, that this only applies to streamlines with $b \leq R_{**}$. For those with $b > R_{**}$, the maximum V_{rad} , which occurs at $x = 0$, is smaller than unity, so that grains on these streamlines do not turn around, although they do slow down temporarily as they go past the star.

The grain density of the inflowing stream follows from mass continuity as:

$$n_d(R) = \frac{n \bar{m} Z_d}{m_d} \left(1 - \frac{R_{**}}{R}\right)^{-1/2}, \quad (\text{C11})$$

where for simplicity we assume a single grain species of mass m_d and dust-gas ratio Z_d . The outflowing stream has exactly the same velocity profile as the inflowing one, apart from a change of sign for those streamlines that turn round. Therefore, in the region where the two streams co-exist ($y \leq R_{**}$, $x > 0$, and $R > R_{**}$), the total density is double that given by equation (C11). This is illustrated in Figure C2.

C3.2 Perpendicular magnetic field

For $\theta_B = 90^\circ$, the guiding center is forced to move at a constant speed in the x direction, so that $x = -v_\infty t$, while the motion in the y direction obeys the ODE:

$$\frac{d^2 y}{dx^2} = \frac{1}{2} R_{**} y (x^2 + y^2)^{-3/2}. \quad (\text{C12})$$

We have been unable to find an analytic solution to this equation, but a numerical solution is shown in Figure C3. When the impact parameter is larger than $b \sim R_{**}$, the trajectories are very similar to in the non-magnetic case (Fig. C1a). As shown in Figure C3b, the interaction of the grain with the radiation field in this large- b regime can be approximated as an impulsive acceleration of magnitude $\sim b^{-2}$ and duration $\sim b$, producing a final y velocity of $\sim b^{-1}$. Since the x velocity is constant, the total deflection angle is also of order $\sim b^{-1}$. The overlap of the outgoing trajectories produces a dense concentration of grains at the inner edge, which is roughly parabolic in shape. However, for $b < R_{**}$ the remorseless advance of the magnetic field does not allow the grains to slow down and turn round, as they do in the non-magnetic and parallel-field cases. As a result, no dense shell forms in the apex region, but instead there is a diffuse minimum in the density of grains around the star due to the high grain velocities reached there. This means that the apparent morphology of a pure dust wave becomes very sensitive to the radial dependence of the grain emissivity. If this is sufficiently steep, then the apex would coincide with the position of the star,

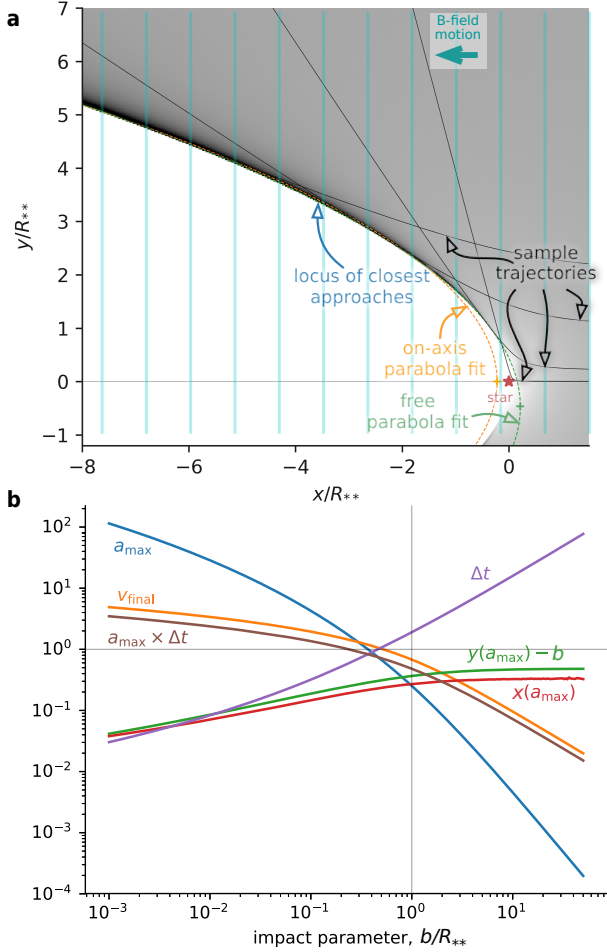


Figure C3. Dust wave formed by action of radiation forces on grains that are tightly coupled to a uniform perpendicular magnetic field. (a) Sample trajectories are shown by thin black lines and the resultant dust density distribution in grayscale. Two parabolic fits to the inner edge of the dust wave in the wing region ($y > R_{**}$) are shown. The orange line shows a simultaneous fit to both wings, while the green line shows a fit to a single wing, in which the parabola apex is not constrained to lie on the axis. The second fit has much smaller residuals, indicating that the overall dust wave shape is “pointier” than a parabola, but this is hard to quantify because the disappearance of the dense shell in the apex region makes it impossible to define R_0 for the bow. (b) Trajectory parameters over a wide range of impact parameters, shown on a log–log scale. Distances are in units of R_{**} , times in units of R_{**}/v_∞ , velocities in units of v_∞ , and accelerations in units of v_∞^2/R_{**} . The grain’s acceleration along the y axis has a maximum value, a_{\max} , which occurs at a position $x(a_{\max})$, $y(a_{\max})$, just before the grain is swept past the star, with a duration (FWHM) of Δt . The grain’s asymptotic y velocity is v_{final} and the fact that this closely tracks $a_{\max} \times \Delta t$ indicates that the majority of the acceleration occurs in a sharp impulse. The curves tend to straight lines at the right side of the graph, which gives the asymptotic scaling relations discussed in the text.

although in practice the presence of a wind-supported bow shock, however small, will complicate the picture.

APPENDIX D: EQUATION OF MOTION FOR GRAINS WITH RADIATION, GAS DRAG, AND MAGNETIC FIELD

Following Draine & Salpeter (1979), the drag force on a grain that is moving at relative velocity $w = w_d - w_{\text{gas}}$ through a partially ionized gas can be written as a sum over each collider species, k , with mass m_k , abundance relative to hydrogen α_k and charge z_k . If the relative speed, $w = |w|$, is normalized to the thermal speed of each species:

$$s_k = (m_k w^2 / 2kT)^{1/2}, \quad (\text{D1})$$

then the magnitude of the force is

$$f_{\text{drag}} = f_* \sum_k \alpha_k \left[G_0(s_k) + z_k^2 \phi^2 \ln(\Lambda/z_k) G_2(s_k) \right], \quad (\text{D2})$$

where f_* is a characteristic thermal force on the grain (see eq. [37]). The dimensionless functions of normalized speed $G_0(s)$ and $G_2(s)$ are given by

$$G_0(s) = \left(s^2 + 1 - \frac{1}{4s^2} \right) \text{erf}(s) + \left(s + \frac{1}{2s} \right) \frac{e^{-s^2}}{\sqrt{\pi}} \quad (\text{D3})$$

$$G_2(s) = \frac{\text{erf}(s)}{s^2} - \frac{2e^{-s^2}}{s\sqrt{\pi}}. \quad (\text{D4})$$

The G_0 term is due to inelastic solid-body collisions in the Epstein limit, and is derived in § 4 of Baines et al. (1965). The G_2 term is due to electrostatic Coulomb interactions, with ϕ being the grain potential in thermal units (eq. [36]) and Λ the plasma parameter. It was first derived in the different context of dynamical friction in stellar systems by Chandrasekhar (1941). Figures 5–7 show example applications to gas–grain drag in a photoionized region.

The grain trajectories presented in § 3.4 and 4.1 are calculated by numerically solving the grain equation of motion:

$$m_d \frac{d^2 r}{dt^2} = f. \quad (\text{D5})$$

The total force f is the sum of radiation, drag, and Lorentz terms:

$$f = \frac{\sigma_d Q_p L}{4\pi R^2 c} \hat{r} - f_{\text{drag}} \hat{w} + \frac{z_d e}{c} w \times \mathbf{B}, \quad (\text{D6})$$

with f_{drag} given by equation (D2) and where \hat{r} is the unit vector in the radial direction and $\hat{w} = w/w$ is the unit vector along the direction of gas–grain relative motion. In the strong magnetic coupling limit (see § 4.1 and C3), the Lorentz term is not included explicitly, but instead the equation of motion is solved for the guiding center by replacing f by its projection along the magnetic field:

$$\tilde{f} = (f \cdot \hat{b}) \hat{b}, \quad (\text{D7})$$

where $\hat{b} = \mathbf{B}/B$.

If distances are measured in units of the radiative turnaround radius, R_{**} (eq. [C2]), and times in units of R_{**}/v_∞ , then the grain acceleration $a_d = f/m_d$ in the non-magnetic case can be written in non-dimensional form as

$$\frac{a_d}{a_{**}} = \frac{R_{**}^2}{2R^2} \hat{r} - C_{\text{drag}} \frac{f_{\text{drag}}}{f_*} \hat{w} \quad (\text{D8})$$

where $a_{**} = v_\infty^2/R_{**}$ is a characteristic acceleration scale and the dimensionless drag constant is

$$C_{\text{drag}} = \frac{4}{Q_p} \left(\frac{c_s \tau_* K_d}{v_\infty \kappa} \right)^2. \quad (\text{D9})$$

A collection of python programs that implement the equations of this appendix is available at <https://github.com/>

[div-B-equals-0/dust-trajectories](#), including programs to generate all the grain trajectory figures of this paper plus additional figures and movies. The integration of equation (D8) is carried out using the python library function `scipy.integrate.odeint`, which wraps the Fortran ODEPACK library (Hindmarsh 1983; Jones et al. 2019).

APPENDIX E: REANALYSIS OF BOW SHOCK SOURCES FROM KOBULNICKY ET AL. (2016, 2017, 2018)

In a series of papers Kobulnicky et al. provide an extensive mid-infrared-selected sample of over 700 candidate stellar bow shock nebulae (Kobulnicky et al. 2016, 2017, 2018, hereafter K16, K17, and K18). For 20 of these sources, reliable distances and spectral classifications are provided (Table 5 of K17 and Tables 1 and 2 of K18), and these are used in § 5, where we discuss the τ - η diagnostic diagram. In this appendix, we outline our treatment and analysis of the data in these catalogs, which differs in some important respects from that of the original authors.

The UV optical depth of the bow shell is obtained (eq. [58]) from the ratio of infrared shell luminosity to stellar luminosity. The inverse of this ratio is given in Table 5 of K17, but we choose to re-derive the values since the spectral classification of some of the sources was revised between K17 and K18. Although K17 found the total shell fluxes from fitting dust emission models to the observed SEDs, we adopt the simpler approach of taking a weighted sum of the flux densities F_ν (in Jy) in three mid-infrared bands:

$$\text{FIR} \approx [2.4(F_8 \text{ or } F_{12}) + 1.6(F_{22} \text{ or } F_{24}) + 0.51 F_{70}] \times 10^{-10} \text{ erg s}^{-1} \text{ cm}^{-2}, \quad (\text{E1})$$

where F_8 is Spitzer IRAC 8.0 μm , F_{24} is Spitzer MIPS 23.7 μm , F_{12} and F_{22} are WISE bands 3 and 4, and F_{70} is Herschel PACS 70 μm . The weights are chosen so that the integral $\int_0^\infty F_\nu d\nu$ is approximated by the sum $\sum_k F_k \Delta\nu_k$, under the assumption that fluxes in shorter (e.g., IRAC 5.8 μm) and longer (e.g., PACS 150 μm) wavebands are negligible. Shell fluxes are converted to luminosities using the assumed distance to each source, and stellar luminosities are taken directly from K18 Table 2, based on spectroscopic classification and the calibrations of gravity and effective temperature from Martins et al. (2005).

In Figure E1 we compare the τ obtained using the shell luminosity as described above with that obtained using the luminosity ratios directly from K17 Table 5. It can be seen that for the majority of sources the two measurements are consistent within a factor of two (gray band). The four furthest-flung outliers can be understood as follows:

Source 67 This has a very poor-quality spectral fit in K17 (see lower left panel of their Fig. 12) and so F_{IR} is overestimated by them by a factor of 10.

Sources 341 and 342 The spectral classes changed from B2V in K17 to O9V and B1V, respectively, in K18, increasing the derived L_* , which lowers τ .

Source 411 The luminosity class changed from Ib (K17) to V (K18), so L_* has been greatly reduced, which increases τ .

K18 derive mass loss rates for their sources using a method that is different from the one that we employ in § 5. Both methods are based on determining the stellar wind ram pressure that supports the bow shell, but K18 do so via the following steps:

- K1. The line-of-sight mass column through the shell is calculated

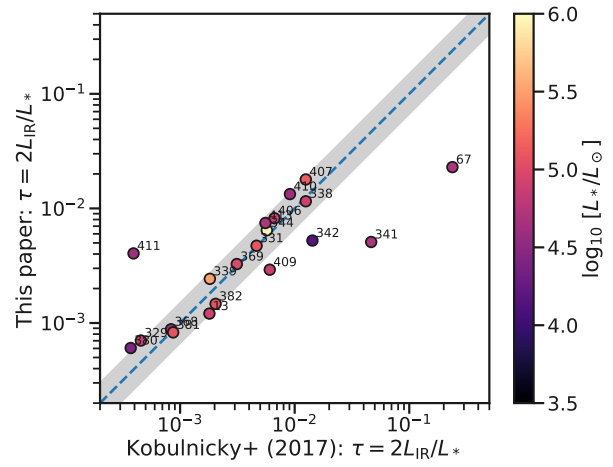


Figure E1. Comparison between shell-to-star luminosity ratios calculated as described in the text (y axis) with those given in K17 (x axis). The blue dashed line signifies equality and the gray band shows ratios between 1/2 and 2.

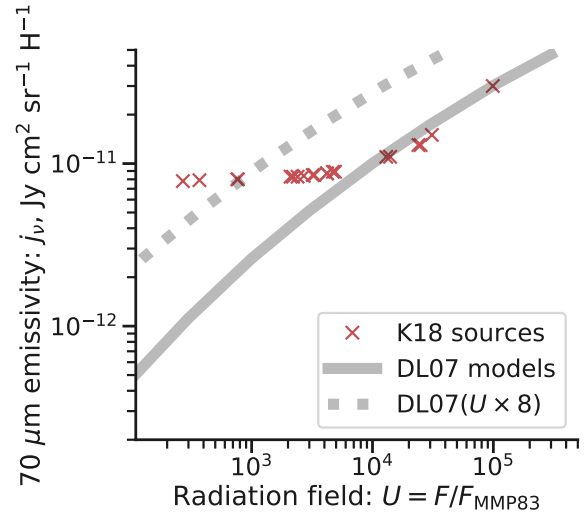


Figure E2. Discrepancies in 70 μm emissivities that we have identified in K18. Red crosses show the emissivities given in K18’s Table 2 as a function of the radiation field U , while the solid gray line shows the emissivities that they claim to be using from Draine & Li (2007). The dashed line shows the emissivities that we believe they should have been using, which correct for the marked difference in spectral energy distribution between OB stars and the Galactic interstellar radiation field (see App. B).

- by combining the peak surface brightness at 70 μm , S_{70} , with a theoretical emissivity per nucleon, $j_{70}(U)$, from Draine & Li (2007): $\Sigma_{\text{los}} = S_{70}/\bar{m}j_{70}(U)$. This depends on knowledge of the stellar radiation field at the shell: $U \propto L_*/R_0^2$.
- K2. The shell density is found from the line-of-sight mass column using an observationally determined “chord diameter”, ℓ , which is assumed to be equal to the depth along the line of sight: $\rho_{\text{sh}} = \Sigma_{\text{los}}/\ell$.
 - K3. The internal ram pressure is equated to the external ram

pressure, which is found by assuming a stream velocity of 30 km s^{-1} and a compression factor of 4 across the outer shock: $P_{\text{stream}} = 0.25\rho_{\text{sh}} \times (30 \text{ km s}^{-1})^2$.

There are clear parallels but also differences between steps K1–K3 and our own steps P1–P3. Our step P1 depends on the total observed infrared flux of the bow combined with an assumption about the grain opacity at ultraviolet wavelengths, while step K1 depends on the peak brightness at a single wavelength combined with an assumption about the grain emissivity at infrared wavelengths. Our step P2 requires an assumption about the relative thickness of the shell, while step K2 is more directly tied to observations.²⁶ On the other hand, step K3 makes a roughly equivalent assumption about the shock compression factor,²⁷ and a further assumption about the stream velocity. These assumptions are not necessary for our step P3, but we do need to assume a value for the shell gas temperature.

In principle, both methods are valid and their different assumptions and dependencies on observed quantities and auxiliary parameters provide an important cross check on one another. However, as explained in detail in Appendix B, the $j_V(U)$ relation depends on the shape of the illuminating SED, which means that the Draine & Li (2007) models require modification when applied to grains around OB stars. In addition, when attempting to replicate the K18 values of j_{70} we find that they only follow the Draine & Li (2007) values for $U > 10^4$, tending to a constant value for weaker radiation fields. The situation is summarized in Figure E2, where the values taken directly from Table 2 of K18 are shown by red crosses, the values they claim to be using are shown by the gray solid line (this curve is consistent with that shown in K18 Fig. 2), and the values they *should* have been using are shown by the gray dashed line.

After correcting the $70 \mu\text{m}$ emissivities in this way, we re-derive the mass loss rates, following the same steps as in K18, which are then used in Figure 14b of § 5. The difference between these corrected mass-loss rates and those published in K18 is shown in Figure E3. It can be seen that sources with $U \approx 10^3$ (darker shading) are relatively unaffected but that sources with stronger radiation fields (lighter shading) have their mass-loss increasingly reduced, as could be surmised from Figure E2. The average reduction is by a factor of about two.

Finally, in Figure E4 we compare our own mass-loss determinations with the corrected K18 values. The plot symbols are shaded according to the physical size of the bow, R_0 . It is apparent that the two methods are broadly in agreement on average, but there is considerable dispersion for individual objects, with only a weak correlation between the results of the two techniques (Pearson correlation coefficient $r = 0.67$). Interestingly, the smaller bows (darker shading) show much better agreement than the larger bows (lighter shading). The five bows with $R_0 > 0.4 \text{ pc}$ (339, 344, 369, 381, 382) show a difference of nearly an order of magnitude, in the sense that our method consistently predicts lower mass-loss rates than K18. For a further five of the sources (380, 407, 409, 410, 411), our method gives only an upper limit to the wind mass-loss rate if

²⁶ Note that there is a relation between the chord length, ℓ , and the shell thickness, h_{sh} , but this depends on the planitude, Π of the bow shape (Tarango-Yong & Henney 2018): $h_{\text{sh}}/R_0 = \Pi(1 - \{1 - [\ell/(2\Pi R_0)]^2\}^{1/2})$.

²⁷ In reality, the compression factor may be larger or smaller than 4, depending on the efficiency of the post-shock cooling (see § 2.5). For instance, for $v = 30 \text{ km s}^{-1}$ as assumed by K18 and $T = 10^4 \text{ K}$, one has a Mach number of $M_0 = 2.63$ and a compression factor of 2.8 for a non-radiative shock (by eq. [27]) or a factor of $M_0^2 = 6.9$ for a strongly radiative one.

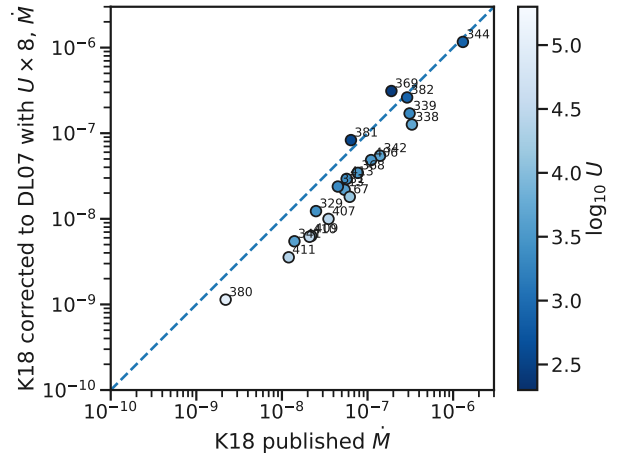


Figure E3. Effects on mass-loss determination of correcting the K18 emissivities. The mass-loss rates from Table 2 of K18 are shown on the x axis, while the corrected values are shown on the y axis. Symbols are color coded by the strength of the radiation field, U . The corrected mass-loss rates are predominantly lower by a factor of roughly 2.

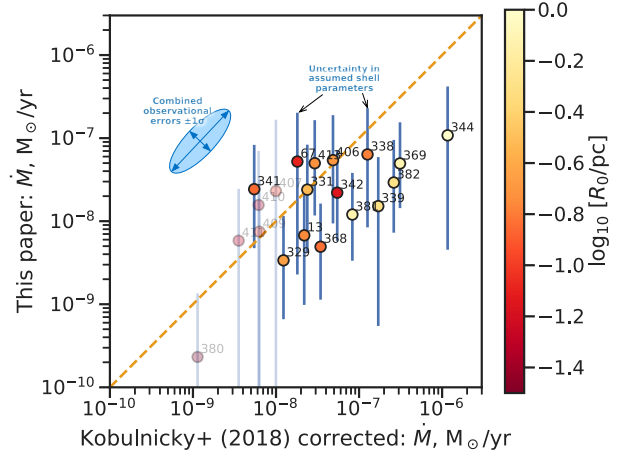


Figure E4. Comparison of the two mass-loss methods: K18 corrected method (x axis) versus our method (y axis). Error bars on the y axis correspond to a factor-three uncertainty in η_{sh} . Sources for which these error bars overlap with the RBW zone are only upper limits for the wind mass-loss rate, and are indicated by faint symbols.

one assumes a factor-three uncertainty in η_{sh} , and these bows are among the smallest in the sample, all with $R_0 < 0.1 \text{ pc}$.

E1 Uncertainty estimates for observational quantities

In this section, we estimate the 1σ uncertainties in observational measurements, which contribute to the uncertainties in the derived quantities: τ , η , and \dot{M} (see § E2 and § 5).

Table E1. Propagation of observational uncertainties to derived quantities

x_i	σ_{x_i}	$J_{x_i}(\tau)$	$J_{x_i}(\eta_{\text{sh}})$	$J_{x_i}(\dot{M})$	$J_{x_i}(\dot{M}_{\text{K18}})$	$J_{x_i}(L_*)$
D	0.08	2	3	3	2	0
L_*	0.18	-1	-2	-1	-0.5	1
F_{IR}	0.12	1	1	1	0	0
I_{70}	0.12	0	0	0	1	0
θ	0.11	0	1	1	2	0
ℓ/R	0.08	0	0	0	-1	0
V_{w}	0.18	0	0	-1	-1	0

E1.1 Distance

Most sources are members of known high-mass clusters with distance uncertainties less than 20% (0.08 dex). The only exception is Source 329 in Cygnus, for which the distance uncertainty is roughly a factor of 2 (Kobulnicky et al. 2018).

E1.2 Stellar luminosity

The stellar luminosity is determined from spectral classification, which makes it independent of distance. Taking a 2000 K dispersion in the effective temperature scale (Martins et al. 2005) gives an uncertainty of 25% in the luminosity, and adding in possible errors in gravity and the effect of binaries, we estimate a total uncertainty in L_* of 50% (0.45 mag or 0.18 dex).

E1.3 Shell flux and surface brightness

We estimate the uncertainty in shell bolometric flux, F_{IR} , by comparing two different methods: model fitting (Kobulnicky et al. 2017) and a weighted sum of the 8, 24, and 70 μm bands (eq. [E1]), giving a standard deviation of 17% (0.07 dex). To this, we add the estimate of 25% for the effects of background subtraction uncertainties on individual photometric measurements (Kobulnicky et al. 2017). The absolute flux calibration uncertainty for both Herschel PACS (Balog et al. 2014) and Spitzer MIPS (Engelbracht et al. 2007) is less than 5%, which is small in comparison. Combining the 3 contributions in quadrature gives a total uncertainty of 0.12 dex. We adopt the same uncertainty for the 70 μm surface brightness.

E1.4 Angular sizes

For the angular apex distance, θ , the largest uncertainty for well-resolved sources is due to the unknown inclination. Tarango-Yong & Henney (2018) show that the dispersion in true to projected distances can introduce an uncertainty of 30% (0.11 dex) in unfavorable cases (e.g., their Fig. 26). For 5 of the 20 sources from Kobulnicky et al. (2018), θ is of order the Spitzer PSF width at 24 μm , so the errors may be larger.

E1.5 Stellar wind velocity

Although this is not strictly an observed quantity for the K18 sample, we will treat it as such since it is estimated per star, based on the spectral type. K18 estimate 50% uncertainty, and we adopt the same here (0.18 dex).

Table E2. Variance–covariance matrix $C_{k,k'}$ for derived quantities

	τ	η_{sh}	\dot{M}	\dot{M}_{K18}	L_*
τ	0.0724	0.1176	0.0852	0.0418	-0.0324
η_{sh}	0.1176	0.2137	0.1489	0.095	-0.0648
\dot{M}	0.0852	0.1489	0.1489	0.1112	-0.0324
\dot{M}_{K18}	0.0418	0.095	0.1112	0.1353	-0.0162
L_*	-0.0324	-0.0648	-0.0324	-0.0162	0.0324

E2 Covariance of derived quantities from propagation of observational uncertainties

Even though errors in the fundamental observed quantities, x_i , are assumed independent,²⁸ errors in the derived quantities, $f_k(x_1, x_2, \dots)$, will not necessarily be so. For the purposes of this paper:

$$x_i \in \{D; L_*; F_{\text{IR}}; I_{70}; \theta; \ell/R; V_{\text{w}}\} \quad (\text{E2})$$

$$f_k \in \{\tau; \eta_{\text{sh}}; \dot{M}; \dot{M}_{\text{K18}}; L_*\}. \quad (\text{E3})$$

Note that L_* appears in both lists because we use it as a graph axis in Figure 14. For the case where each f_k is a simple product of powers of the x_i , the propagation of errors reduces to linear algebra of log quantities. This is exactly true for τ and η_{sh} , but only approximately so for \dot{M} and \dot{M}_{K18} .²⁹ We define $J_{x_i}(f_k)$ as the elements of the Jacobian matrix of logarithmic derivatives $d \ln f_k / d \ln x_i$, which are given for our quantities in Table E1. Then, the elements of the variance–covariance matrix for the derived parameters are

$$C_{k,k'} = \sum_i J_{x_i}(f_k) \sigma_{x_i}^2 J_{x_i}(f_{k'}), \quad (\text{E4})$$

where the σ_{x_i} are the rms dispersions in x_i , measured in dex. In Figure E5 we give example python code for calculating this matrix, using the σ_{x_i} derived in § E1.1–E1.5 for the K18 sources (second column of Tab. E1), with results given in Table E2. It can be seen that many of the off-diagonal elements are of similar magnitude to the diagonal elements, which is an indication of significant correlations between the errors in the different parameters.

For any particular pair of derived quantities, f_m and f_n , one can find the *error ellipse* that characterises the projection of observational errors onto the $f_m - f_n$ plane. The ellipse is characterized by standard deviations along major and minor axes, σ_a , σ_b , together with the angle θ_a between the f_m axis and the ellipse major axis. These are given via the eigenvalues and eigenvectors of the relevant 2×2 submatrix of the covariance matrix:

$$\sigma_a^2 = \frac{1}{2} \left\{ C_{m,m} + C_{n,n} + \left[(C_{m,m} + C_{n,n})^2 - 4C_{m,n}^2 \right]^{1/2} \right\} \quad (\text{E5})$$

$$\sigma_b^2 = \frac{1}{2} \left\{ C_{m,m} + C_{n,n} - \left[(C_{m,m} + C_{n,n})^2 - 4C_{m,n}^2 \right]^{1/2} \right\} \quad (\text{E6})$$

$$\theta_a = \frac{1}{2} \arctan \left(\frac{2C_{m,n}}{C_{m,m} - C_{n,n}} \right). \quad (\text{E7})$$

For instance, Table E3 shows the resultant error ellipse parameters (shown in blue on the respective graphs) for the relations plotted in Figures 13, 14ab, and E4.

²⁸ It is of course true that F_{IR} and I_{70} are not completely independent from one another, but this does not matter since we consider only derived quantities that are a function of one or the other, not both.

²⁹ For \dot{M} it is true for $\eta_{\text{sh}} \gg 1.25\tau$ and for \dot{M}_{K18} it is true in the limit that the grain emissivity can be expressed as a power law in U .

Table E3. Error ellipse parameters for particular pairs of derived quantities

f_m	f_n	σ_a	σ_b	$\theta_a, {}^\circ$	Figure
τ	η	0.529	0.077	60.5	13
L_*	\dot{M}	0.397	0.155	-75.5	14a
L_*	\dot{M}_{K18}	0.371	0.173	-81.3	14b
\dot{M}_{K18}	\dot{M}	0.503	0.175	46.7	E4

```
import numpy as np
sig = np.diag([0.08, 0.18, 0.12, 0.12, 0.11, 0.08, 0.18])
J = np.array([
    [2, -1, 1, 0, 0, 0, 0],
    [3, -2, 1, 0, 1, 0, 0],
    [3, -1, 1, 0, 1, 0, -1],
    [2, -0.5, 0, 1, 2, -1, -1],
    [0, 1, 0, 0, 0, 0, 0]
])
C = J @ sig**2 @ J.T
```

Figure E5. Snippet of Python code that calculates the covariance matrix of Table E2. The last line implements equation (E4) by a triple matrix product of the Jacobian matrix J , the square of a diagonal matrix of observational standard deviations sig , and the transpose of J .

E3 Notes on particular sources

E3.1 Source 380, HD 53367, V750 Mon

This is a Herbig Be star with spectral type B0V–B0III and mass 12 to $15 M_\odot$, which shows long-scale irregular photometric variability (Tjin A Djie et al. 2001; Pogodin et al. 2006) together with cyclic radial velocity variations, which are interpreted as an eccentric binary with a $5 M_\odot$ pre-main-sequence companion. It is located outside the solar circle and, although it was originally classified as part of the CMa OB association at about 1 kpc (Tjin A Djie et al. 2001), more recent estimates put it much closer. K18 assume a distance of 260 pc, based on Hipparcos measurements (van Leeuwen 2007), but its Gaia DR2 parallax (Gaia Collaboration et al. 2016, 2018; Luri et al. 2018) puts it closer still at (140 ± 30) pc.³⁰

Quireza et al. (2006b) report a kinematic distance to the associated H II region IC 2177 (G223.70–1.90) of 1.6 kpc, based on LSR radio recombination line velocity of 16 km s^{-1} (Quireza et al. 2006a) and the outer Galaxy rotation curve of Brand & Blitz (1993). However, given the dispersion in peculiar velocities of star-forming clouds (7 km s^{-1} to 9 km s^{-1} , Stark 1984) and likely streaming motions of the ionized gas ($\approx 10 \text{ km s}^{-1}$, Matzner 2002; Lee et al. 2012), this is still consistent with a much smaller distance, which would also help in bringing the radio continuum-derived nebular electron density into agreement with the value ($\approx 100 \text{ cm}^{-3}$) derived from the optical [S II] line ratio (Hawley 1978).

Fairlamb et al. (2015) derive a distance of (340 ± 60) pc from combining a spectroscopically determined effective temperature, gravity, and reddening with photometry and pre-main sequence evolutionary tracks. They also determine a luminosity of $(13\,000 \pm 1000) L_\odot$, which is only half that assumed by K18, and would have to be even lower to bring the photometry into concordance with the Gaia distance. Alternatively, the luminosity could remain the same if the total-to-selective extinction ratio were higher than

³⁰ Median and 90% confidence interval, estimated from Bayesian inference using an exponential density distribution with scale length of 1350 pc as a prior (see <https://github.com/agabrown/astrometry-inference-tutorials/>).

the $R_V = 3.1$ assumed by Fairlamb et al. (2015). Taking $R_V = 5.5$ instead, as in Orion, would give $A_V = 3.34$ and a predicted V magnitude of 6.7 if we assume $L_4 = 1.3$, $D = 170$ pc (furthest distance in Gaia 90% confidence interval) and $T_{\text{eff}} = 29.5 \text{ kK}$ (Fairlamb et al. 2015) for a bolometric correction of -2.86 (Nieve 2013). The observed brightness varies between $V = 6.9$ and 7.2, which is still at least 20% fainter than predicted, but this is the best that can be achieved without rejecting the Gaia parallax distance entirely.

A final sanity check can be performed by considering the free-free radio continuum flux of V750 Mon’s surrounding H II region, which, after converting to a luminosity, should be proportional to the total recombination rate in the nebula and therefore, assuming photoionization equilibrium and negligible dust absorption in the ionized gas, also proportional to the ionizing photon luminosity of the star. Quireza et al. (2006b) report a flux density of 6 Jy at 8.6 GHz for G223.70–1.90, as compared with a flux density of 260 Jy for the Orion Nebula using the same instrumental setup. Assuming an ionizing photon luminosity of $S_{49} = 1$ and distance 410 pc for Orion, therefore implies $S_{49} = 0.0027(D/140 \text{ pc})^2$ for V750 Mon. Using the ionizing flux curves from Fig. 4 of Sternberg et al. (2003), this translates to a bolometric luminosity of $L_4 = 0.96(D/140 \text{ pc})^2$, which is consistent with the Fairlamb et al. (2015) value if we take a distance towards the high end of the Gaia range.

This paper has been typeset from a TeX/LaTeX file prepared by the author.